(Non-)linear Spectroscopy Based on Classical Trajectories

Master-Thesis
angefertigt am Institut für Physik
der Mathematisch-Naturwissenschaftlichen Fakultät
der Universität Rostock

vorgelegt von

Tobias Zentel, geb. am 16. September 1986 in Mainz

Rostock, 11. September 2012

https://doi.org/10.18453/rosdok_id00000262

1. Gutachter Prof. Dr. O. Kühn
2. Gutachter:Dr .S. Ivanov

Adresse: Universität Rostock
Institut für Physik
18051 Rostock

Contents

1. Introduction

1.1. Quantum Dynamics and Spectroscopy

As physicists we try to describe the world around us from the macroscopic objects like galaxies down to the smallest building blocks of our universe. In this thesis effects on the microscale will be discussed. Atoms and molecules are quantum mechanical objects and do not behave in a manner easily understandable to humans. One tool to investigate the dynamical properties of molecules is spectroscopy, which in essence is a succession of light-matter interactions. The interaction of incoming photons with the sample brings the system out of equilibrium and to reach back to the equilibrium state the molecules emit photons or undergo vibrational relaxation. The simplest form of spectroscopy is an absorption experiment. Light is shone on the object under study and the properties of the emitted light are analyzed. To characterize the dynamics of atoms the time resolution has to be on the order of femtoseconds, the timescale on which nuclei move. Advances in recent years in LASER technology, especially the development of Ti:Sa lasers with passive mode locking, pushed the limits of time resolution to a few femtoseconds. As discussed later, most prominent effects are genuinely non-linear and have to be accessed by non-linear spectroscopy [1].

The ultimate goal of this thesis is to establish a protocol for the simulation of (non-) linear spectra of molecular systems, in particular ionic liquids. The description of molecules involves solving the time-dependent Schrödinger equation, but for a somewhat large system this is already computationally not possible. A method that is applicable to larger systems must be efficient and scale well with the system size. The best starting point to fulfill these requirements is to establish a simulation method based on purely classical calculations.

1.2. Non-linear Spectroscopy

The linear relationship between polarization $\vec{P}$ and electromagnetic field $\vec{E}$, often assumed valid in absorption experiments, is just a first order approximation. This approximation is no longer valid for high energy densities, mostly found in focused laser fields. This was first observed in experiment by Franken *et al.* [2], who were able to observe second harmonic generation using laser fields, that is the conversion of two photons into one photon with the doubled frequency. To describe this and other new effects Bloembergen *et al.* [3] added an anharmonic term to the wave equation. As a result, effects quadratic in the field $\vec{E}$ are described. The second order term $\vec{P}^{(2)}$, quadratic in the field, gives rise to many existing effects [1], like two-photon absorption, three-wave mixing and frequency up/down conversion. If we consider the third order polarization the optical Kerr effect and four-wave mixing become possible to mention but two. In general, the polarization $\vec{P}$ is split into a linear and non-linear term

$$\vec{P}[\vec{E}] = \vec{P}_{\mathrm{L}}[\vec{E}] + \vec{P}_{\mathrm{NL}}[\vec{E}],$$

where the non-linear polarization $\vec{P}_{\mathrm{NL}}[\vec{E}] \equiv \vec{P}^{(2)} + \vec{P}^{(3)} + \ldots$ consists of all higher than first order terms in the field.

In this context, n-wave mixing is a $n-1$ order process, where $n-1$ incoming waves interact with the medium to produce one response signal field, summing to n participating waves. A four-wave mixing process is illustrated in Fig. 1.1. Due to the momentum conservation the process is governed by phase matching as well as by frequency matching due to the energy conservation

$$\sum_{i=1}^{4} \vec{k}_i = 0 \qquad , \qquad \sum_{i=1}^{4} \omega_i = 0 \ .$$

For the three incoming fields with wave vectors $\vec{k}_i$ and frequencies ω_i the outgoing signal field has 6 possible wave vector directions $\vec{k}_s = \pm\vec{k}_1 \pm \vec{k}_2 \pm \vec{k}_3$ and frequencies $\omega_s = \pm\omega_1 + \pm\omega_2 \pm \omega_3$.

For the present four-wave mixing is mostly interesting, because it is directly linked to 2d spectroscopy and CARS (coherent anti-Stokes Raman spectroscopy) that are methods used by experimental collaborators of our group. In 2d spectroscopy three femtosecond pulses separated in time interact with the sample and create a signal. The measured intensity is then dependent on the time delays of the incoming pulses. 2d spectra are

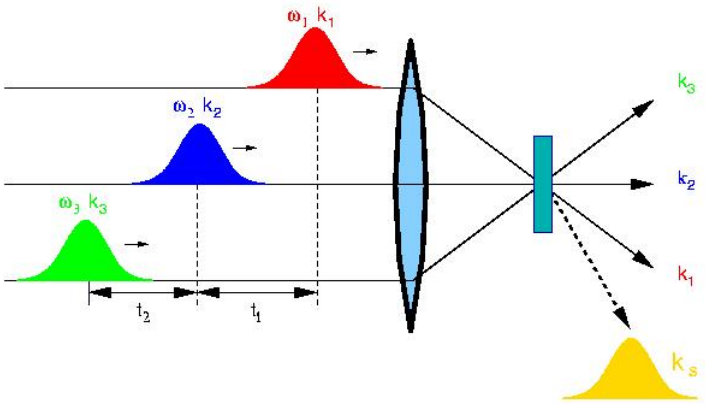

Figure 1.1.: A schematic illustration of four-wave mixing. Three incoming photons interact with the medium, which emits a signal photon (yellow). The direction of the signal can be controlled via phase matching condition.[1]

Fourier transforms of the collected data with respect to the time interval between the first two pulses t_1, referred to as coherence time, and the time between the signal and the last incoming pulse t_3. The so-called population time t_2 between the second and third pulse is fixed [4] and 2d spectrum is therefore measured for different population times t_2 in order to study the dynamics of the system.

In the following a method to calculate the 2d and other non-linear spectra will be established. A new method has to be tested on model systems before application to molecular systems. One test system will be the 1d Morse potential, because it is often used in molecular physics to describe bonds and is analytically solvable. The dynamics in a Morse potential is integrable and quasi-periodic. To work out the influence of chaos, a property most likely found in molecular systems, onto the method a second, chaotic model system, namely a Hénon Heiles potential is used.

1.3. Ionic Liquids

The new products (plastics, fine chemicals, pharmaceuticals) made available by industrial chemical synthesis greatly increased the quality of life for many humans. Still the current modern technology relies heavily on wasteful processes and the consumption

[1] http://www.mbi-berlin.de/de/research/projects/2-04/subprojects/Subproject5/p3_experiment.jpg (28.8.2012)

of natural resources. A sustainable chemical industry needs solvents, that are efficient, nontoxic and nonvolatile. Big economical and ecological interest lies on replacing conventional, potentially dirty and/or inefficient, organic solvents by 'green' solvents [5]. Ionic liquids are a hot topic in this context and have made their first commercial appearances in recent years.

To make an example, Zhao *et al.* [6] investigated the solvation of cellulose, the primary product of plants in 27 different ionic liquids. Solvents based on the cation [C_2mim] reach up to 18wt% (= weight percent) solubility. It is worth mentioning that conventional solvents perform poorly on cellulose, and the construction of new efficient solvents is highly desirable.

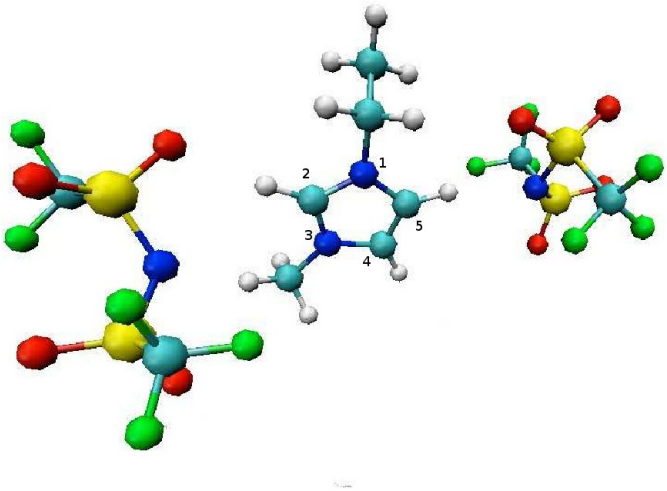

Figure 1.2.: The cation [C_2mim] in the middle surrounded by two anions [NTf_2].

What makes ionic liquids so special? While conventional liquids are governed primarily by hydrogen bonds (H-bonds) and van der Waals forces, the ionic character of ionic liquids introduces particularly strong Coulomb forces to the system that lead to a distinctly different behavior and opens up possibilities for new applications. Presumably there exists about one trillion room temperature ionic liquids accessible [5], many of them are inflammable, stable and non-volatile. As pointed out in [7], high polarity and non-volatility of ionic liquids together with the fact that they are mostly good solvents, make them very promising candidates for green solvents in synthesis. Yet, the underlying mechanism on the atomistic level responsible for the unique properties has not been

understood. In particular it is debated to what extend H-bonds play a role in these complex systems and how they interplay with Coulomb forces. A deeper understanding on the microscopic level is needed to foster the full potential of ionic liquids and pave the road towards ionic liquids with tunable properties.

1.4. Alkylmethylimidazolium

Imidiazolium based cations are very common in ionic liquids and hence in the following the focus is exemplarily set on 1-ethyl-3-methyl-imidazolium[C_2mim] and bis(trifluoromethanesulfonyl)imide [NTf_2] (see Fig. 1.2). The cation consists of a five-member ring consisting of three carbon and two nitrogen atoms with two alkyl side chains attached to the latter. The nitrogen atom with the longer alkyl chain is referred to as N(1) atom, the methyl group is on the N(3) atom.

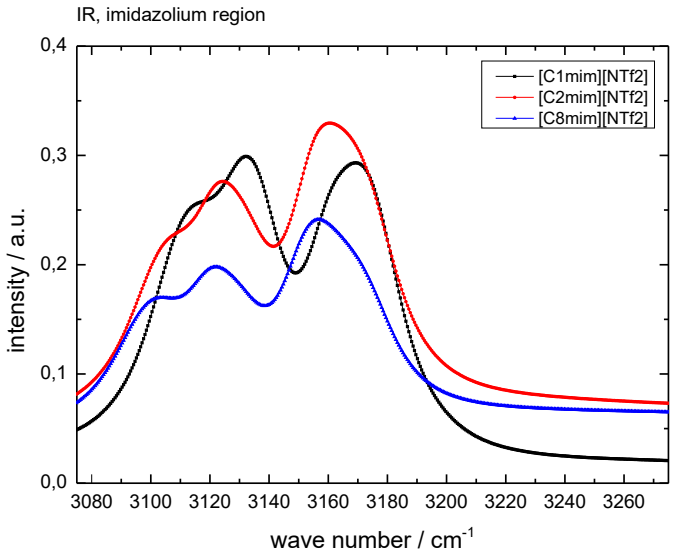

Figure 1.3.: IR absorption spectrum for different chain lengths on the cation [8]

Experimental results make a strong case for the significance of H-bonds, that can occur between the imidazolium ring based hydrogen atoms and the oxygen or nitrogen atoms of the anion. An H-bond signature is the redshift of the C-H stretching vibrations together with decrease in the cation-anion distance. In [8] Raman, CARS and IR absorption spectra, see Fig. 1.3, of [$C_n$mim] [NTf_2] were taken and bands were assigned. In particular the C(4)-H and C(5)-H were found at 3180cm^{-1} and 3160cm^{-1}. The shift to

the red of the C(2)-H stretch with respect to C(4/5)-H stretch corresponds to a stronger H-bond than on the other side of the ring, but it is still categorized as moderate.

The C(2)-H stretch is Fermi resonant with in ring vibrations and is assigned to the two features at 3120cm^{-1}. Grondin *et al.* [9] characterize the bands very differently, namely all three C-H stretches are assigned to the peak around 3160cm^{-1}, while the signal at 3120cm^{-1} is attributed exclusively to the Fermi-resonant overtones of ring vibrations. This work is aiming at results elucidating the band assignment and H-bond properties in ionic liquids.

In chapter 2 response functions will be introduced to describe the spectroscopic signal and in chapter 3 an overview of different methods of molecular dynamics (MD) is given before commenting on the computational details and presenting results.

2. Theory

2.1. Interaction Representation

In order to describe the time evolution of a (by laser) perturbed system quantum mechanical time evolution operators in different representations are introduced. We start with a wave function $\Psi(t)$ that obeys the time-dependent Schrödinger equation

$$i\hbar\frac{d}{dt}\Psi(t) = \hat{H}\Psi(t) \tag{2.1}$$

with the Hamiltonian $\hat{H}$ of the system. Expectation values of an operator $\hat{O}$ are defined as

$$\langle\Psi(t) \mid \hat{O} \mid \Psi(t)\rangle = \mathrm{Tr}(\hat{O}\hat{\rho}(t)) \ ,$$

where the density matrix is $\rho(t) = |\Psi(t)\rangle\langle\Psi(t)|$. In the Schrödinger picture the wave functions are time-dependent and operators are time-independent. In the equivalent description of quantum dynamics operators are time-dependent and wave functions time-independent. To switch to this so-called Heisenberg representation, the time evolution operator $\hat{U}(t, t_0)$ is used, which is obtained by integrating Eq. 2.1

$$\hat{U}(t, t_0) = \exp(-\frac{i}{\hbar}\hat{H}(t - t_0)) \tag{2.2}$$

The wave function and operators can be obtained from the Schrödinger representation by

$$\Psi(t) = U(t, t_0)\Psi^{\mathrm{H}} \qquad \text{and} \qquad \hat{O}^{\mathrm{H}}(t) = U^{\dagger}(t, t_0)\hat{O}U(t, t_0)$$

where dagger denotes the adjoint operators. In the following it will be more suitable to employ the **interaction representation** or Dirac representation. As a first step the

Hamiltonian is split into two parts

$$\hat{H}(t) = \hat{H}_0 + \hat{V}(t)\,,$$

a time-dependent perturbation $\hat{V}(t)$ and the unperturbed Hamiltonian $\hat{H}_0$. In this representation both the wave function and the operators, are time dependent. The time evolution of the wave function in interaction representation $\Psi^{\mathrm{I}}(t)$ is governed by the $\hat{S}$-operator

$$\Psi^{\mathrm{I}}(t) = \hat{S}(t, t_0)\Psi_0$$

with

$$\hat{S}(t, t_0) = \hat{T}\exp\left(-\frac{i}{\hbar}\int_{t_0}^{t} dt'\hat{V}^{\mathrm{I}}(t')\right), \tag{2.3}$$

$\hat{T}$ being the time ordering operator. Eq. 2.3 represents a concise notation for an infinite perturbation series. The time evolution operator in the interaction representation only depends on the unperturbed Hamiltonian and evolves according to

$$\hat{U}_0(t, t_0) = \exp(-\frac{i}{\hbar}\hat{H}_0(t - t_0)).$$

The Schrödinger and Dirac representations are connected only by $\hat{U}_0$ via

$$\Psi(t) = \hat{U}_0(t, t_0)\Psi^{\mathrm{I}}(t) \qquad \text{and} \qquad \hat{O}^{\mathrm{I}}(t) = \hat{U}_0^{\dagger}(t, t_0)\hat{O}\hat{U}_0(t, t_0) \tag{2.4}$$

whereas the original Heisenberg time evolution operator in Eq. 2.2 is regained by the combination

$$\hat{U}(t, t_0) = \hat{U}_0(t, t_0)\hat{S}(t, t_0). \tag{2.5}$$

In the following the interaction picture is used to derive a formalism that describes the response of a perturbed system, and Eq. 2.3 is expanded to the desired order, leading to the corresponding order in polarization.

2.2. Quantum Response Functions

The observable accessible through spectroscopic experiments is the $n-$th order polarization [10], thus time evolution of the polarization after the interaction with the field

is of interest here. Let's assume a homogeneous medium where $\hat{\mu}$ stands for the dipole moment operator of a single molecule. Then the polarization $P(t)$ is the sum of the expectation values of the molecular dipole moment operators [10]

$$\vec{P}(t) = n_{\text{mol}} \text{Tr}\left[\hat{\rho}(t)\hat{\mu}\right], \tag{2.6}$$

with the density n_{mol}. As it was mentioned in the introduction, a system, in equilibrium befor the light-matter interaction, is coupled to the incoming laser fields $\vec{E}$ via the dipole moment operator, so the perturbative part $\hat{V}(t)$ of the Hamilton operator is [1]

$$\hat{V}(t) = -\hat{\mu}E(t),$$

with $E(t)$ being the transverse part of the field $\vec{E}(t)$. The time evolution of the density matrix reads as

$$\hat{\rho}(t) = |\Psi(t)\rangle\langle\Psi(t) = \hat{U}(t,t_0)\hat{\rho}_{\text{eq}}\hat{U}^{\dagger}(t,t_0) = \hat{U}_0(t,t_0)\hat{S}(t,t_0)\hat{\rho}_{\text{eq}}\hat{S}^{\dagger}(t,t_0)\hat{U}_0^{\dagger}(t,t_0)\ . \tag{2.7}$$

and the dipole moment according to Eq. 2.4 as

$$\hat{\mu} = \hat{U}_0(t,t_0)\hat{\mu}^{\text{I}}(t)\hat{U}_0^{\dagger}(t,t_0).$$

Substitution of this and Eq. 2.5 into Eq. 2.6 and using the cyclic invariance of the trace leads to

$$P(t) = n_{\text{mol}} \text{Tr}\left[\hat{\rho}_{\text{eq}}\hat{S}^{+}(t,t_0)\hat{\mu}^{\text{I}}(t)\hat{S}(t,t_0)\right]. \tag{2.8}$$

As required by the experiment, the focus is put on calculating the individual n-th order polarization only, thus the operator $\hat{S}(t,t_0)$ in Eq. 2.8 is therefore expanded to the n-th order

$$\hat{S}(t,t_0) \to 1 + \hat{S}^{(1)}(t,t_0)) + \hat{S}^{(2)}(t,t_0) + \cdots + \hat{S}^{(n)}(t,t_0)$$

and all n-th order terms are collected. The result for the n-th order polarization can be written in terms of the response function $R^{(n)}(\tau,\tau_n,...,\tau_1)$ and n external fields $\vec{E}$ acting at times τ_i, see appendix and [11]

$$P^{(n)}(\tau) = \int_0^{\tau} d\tau_n \int_0^{\tau_n} d\tau_{n-1} \ldots \int_0^{\tau_2} d\tau_1 E(\tau_1)\ldots E(\tau_n) R^{(n)}(\tau,\tau_n,\ldots,\tau_1).$$

The response function $R^{(n)}$ is an n-point correlation function, that with the help of the notation $< \bullet >:= \mathrm{Tr}\left[\hat{\rho}_{\mathrm{eq}} \bullet\right]$, reads as

$$R^{(n)}(\tau, \tau_n, \ldots, \tau_1) = \left(\frac{i}{\hbar}\right)^n \left\langle [[\hat{\mu}^{\mathrm{I}}(\tau), \hat{\mu}^{\mathrm{I}}(\tau_n)], \ldots \hat{\mu}^{\mathrm{I}}(\tau_1)] \right\rangle \ . \tag{2.9}$$

Note that $R^{(n)}(\tau, \ldots, \tau_1)$ is not a function of the position r, since we assumed the medium to be homogeneous. For the present purpose, the focus is put on the first order (linear) response function and the third order (non-linear) response function. The second order is not of interest here, since the second order polarization $P^{(2)}$ vanishes in most cases due to the inversion symmetry, note that it is useful to study surfaces however. In the following it will be more convenient to use the time intervals between interactions t_i instead of the absolute times τ_i.

The linear response function is comprised of just a single commutator of the dipole moments at the different times, namely the time of the photon absorption, here set to zero, and the time of the photon emission, after the interval t

$$R^{(1)}(t) = \frac{i}{\hbar} \langle [\hat{\mu}(t), \hat{\mu}(0)] \rangle \, . \tag{2.10}$$

Here and in the following the superscript I is left out, because the only dipole moment operator with time-dependence used in the following is in the interaction representation. It is inconvenient to calculate linear response directly from Eq. 2.10 and the correlation functions $C(t)$ are used instead [12]

$$R^{(1)}(t) = \frac{i}{\hbar} \left(\langle \hat{\mu}(t)\hat{\mu}(0) \rangle - \langle \hat{\mu}(0)\hat{\mu}(t) \rangle \right) = \frac{i}{\hbar} \left\langle C_{\mu\mu}(t) - C^{\dagger}_{\mu\mu}(t) \right\rangle$$

with the correlation function

$$C_{xy}(t) = \langle \hat{x}(t)\hat{y}(0) \rangle \, .$$

The Fourier-transformed correlation functions fulfill the detailed balance condition

$$C_{xy}(\omega) = \exp\left(\frac{\hbar\omega}{kT}\right) C_{xy}(-\omega)$$

which would require special care upon taking the classical limit in the next section.

The non-linear response function

$$R^{(3)}(t_3, t_2, t_1) = \left(\frac{i}{\hbar}\right)^3 \langle [[[\hat{\mu}(t_3 + t_2 + t_1), \hat{\mu}(t_2 + t_1)], \hat{\mu}(t_1)], \hat{\mu}(0)] \rangle \tag{2.11}$$

becomes a four-point correlation function of the dipole moments.

In this section we expressed the individual n-th order polarization through the n-th order response function $R^{(n)}$, which has to be evaluated to calculate (non-) linear spectra, and this is the scope of the next section

2.3. Classical Response Functions

As has been pointed out before, spectra are to be calculated through classical molecular dynamics, therefore we need to find a classical mechanical expression for the response functions. Upon replacing quantum commutators in the n-th order quantum response function Eqs. 2.10 and 2.11 by Poisson brackets and taking the limit $\hbar \to 0$ the n-th order classical response function $R_{\mathrm{cl}}^{(n)}$ is obtained. The two orders we are interested in read as [13]

$$R_{\mathrm{cl}}^{(1)}(t) = -\left\langle \{\mu(t), \mu(0)\} \right\rangle_{\mathrm{cl}} \tag{2.12}$$

and

$$R_{\mathrm{cl}}^{(3)}(t_3, t_2, t_1) = -\left\langle \{\{\{\mu(t_3 + t_2 + t_1), \mu(t_2 + t_1)\}, \mu(t_1)\}, \mu(0)\} \right\rangle_{\mathrm{cl}}. \tag{2.13}$$

Note, that the quantum ensemble average in the QM response function is replaced by the canonical ensemble average $< \ldots >_{\mathrm{cl}}$. The Poisson bracket contains derivatives with respect to different times, this makes the evaluation of equations 2.12 and 2.12 difficult. If $\Gamma = (q_1, \cdots, q_{3N}, p_1, \cdots, p_{3N})^T$ comprising of all phase space variables, the Poisson bracket of two arbitrary vectors A and B stands for

$$\{A, B\} = \frac{\tilde{\partial} A(t_1)}{\partial \Gamma_{t_0}} \mathbf{J} \frac{\partial B(t_0)}{\partial \Gamma_{t_0}}, \tag{2.14}$$

where tilde denotes the matrix transpose and $\mathbf{J}$ stands for the symplectic matrix

$$\mathbf{J} = \begin{pmatrix} \mathbf{0} & \mathbf{I} \\ \mathbf{-I} & \mathbf{0} \end{pmatrix}. \tag{2.15}$$

One introduces the stability matrix $\mathbf{M}(t,t')$, whose n-th order elements are [11]

$$\mathbf{M}^{(n)}_{i,j..k}(t,t_1,\ldots,t_n) = \frac{\partial^n \Gamma_i(t)}{\partial\Gamma_j(t_1)\ldots\partial\Gamma_k(t_n)}.$$

In particular the first order stability matrix $\mathbf{M}$ is written down as

$$\mathbf{M}(t,t') = \frac{\tilde{\partial}\Gamma_t}{\partial\Gamma_{t'}} = \begin{pmatrix} \frac{\partial \mathbf{q}_t}{\partial \mathbf{q}_{t'}} & \frac{\partial \mathbf{q}_t}{\partial \mathbf{p}_{t'}} \\ \frac{\partial \mathbf{p}_t}{\partial \mathbf{q}_{t'}} & \frac{\partial \mathbf{p}_t}{\partial \mathbf{p}_{t'}} \end{pmatrix},$$

with q and p being positions and their conjugate momenta, respectively. Its matrix elements show how coordinates and momenta of the system respond at a time t to small initial deviations at an earlier time t' and thus quantify the stability of classical trajectories with respect to changes in their initial conditions [14]. It is claimed that the matrix elements **diverge exponentially** in chaotic systems and linearly in quasiperiodic systems [14]. It will be discussed later that matrix elements in quasiperiodic systems in fact oscillate. Since response functions are linked directly to stability matrices it is suggested that response functions can be used as a measure of classical chaos [15].

This divergence of matrix elements implies the divergence of the respective response function. Van Kampen [34] pointed out that the response functions approach leads to a failure at longer times, because perturbation theory is not valid in chaotic systems at long times. Nevertheless the approach works well, as can be seen from results published using classical response functions. The divergence can be controlled by **averaging over phase space**. The different divergent contributions from each trajectory cancel out and the response functions are mostly nicely behaved. But when calculating the response with a given accuracy, the number of needed trajectories increases exponentially with the simulation time [16].

2.3.1. Linear Response Functions

With the stability matrix introduced we can rewrite the response in terms of $\mathbf{M}(t_1+t_0,t_0)$. It follows for $R^{(1)}_{\mathrm{cl}}(t)$

$$\begin{aligned} R^{(1)}_{\mathrm{cl}}(t) &= -\langle\{\mu(t),\mu(0)\}\rangle = -\left\langle \frac{\tilde{\partial}\mu(t)}{\partial\Gamma_0}\mathbf{J}\frac{\partial\mu(0)}{\partial\Gamma_0}\right\rangle \\ &= -\left\langle \frac{\tilde{\partial}\mu(t)}{\partial\Gamma_t}\mathbf{M}(t,0)\ \mathbf{J}\frac{\partial\mu(0)}{\partial\Gamma_0}\right\rangle . \end{aligned} \tag{2.16}$$

All quantities involved in derivatives are now with respect to the same time arguments and can be calculated for the price of evaluating the stability matrix. Having in mind the properties of stability matrices, the use of Eq. 2.12 is not common to calculate linear spectra. Instead, the classical correlation function $\xi(t)$

$$\xi(t)_{\mu\mu} = \langle \mu(t)\mu(0) \rangle_{\mathrm{cl}} \,. \tag{2.17}$$

is used. But in the frequency domain the detailed balance condition of the quantum correlation are lost. Therefore one constructs in the frequency domain [12]

$$C_{uv}(\omega) = \frac{2}{1+\exp(-\frac{\hbar\omega}{kT})}\xi_{uv}(\omega) \tag{2.18}$$

$$C_{uv}(-\omega) = \frac{2}{1+\exp(\frac{\hbar\omega}{kT})}\xi_{uv}(\omega), \tag{2.19}$$

and the detailed balance condition is then fulfilled.

A direct connection to the fluctuation-dissipation theorem can be made [15], when using the property of a canonical distribution for an arbitrary vector A

$$\{A, \rho_{\mathrm{eq}}\} = -\beta \dot{A} \rho_{\mathrm{eq}}. \tag{2.20}$$

The linear response can then be formulated as

$$R^{(1)}_{\mathrm{cl}}(t) = \beta \left\langle \mu(t)\dot{\mu}(0) \right\rangle_{\mathrm{cl}} , \tag{2.21}$$

which connects the linear response of a system due to perturbations to the one due to statistical fluctuations.

2.3.2. Non-linear Response Functions

The same general procedure is used again to obtain the non-linear response function. But care has to be taken of the nested brackets. Just using Eq. 2.14 to write out the Poisson brackets leads to high order stability matrices, which diverge faster than lower order stability matrices. As described in [11] it is possible to recast response functions in a way that reduces the order of the highest occurring stability matrix. This is done by switching from the Schrödinger picture to a so-called intermediate picture through

integration by parts

$$\int d\Gamma\{A,B\}C = \int d\Gamma A\{B,C\} \tag{2.22}$$

and moving the time evolution from the density matrix to the dipole moments. This way, to calculate **third** order response only **first** order stability matrices and easy-to-handle correlation functions are required. Still even first order stability matrices diverge for long times and possibly produce wrong response functions. Using Eq. 2.22, the response function Eq. 2.13 becomes

$$\begin{aligned} R^{(3)}_{\mathrm{cl}}(t_3,t_2,t_1) &= -\Big\langle\{\{\{\mu(t_3),\mu(t_2)\},\mu(t_1)\},\mu(0)\}\Big\rangle \\ &= -\int \mathrm{d}p \int \mathrm{d}q\ \{\{\{\mu(t_3),\mu(t_2)\},\mu(t_1)\},\mu(0)\}\rho_{\mathrm{eq}} \\ &= -\int \mathrm{d}p \int \mathrm{d}q\ \{\{\mu(t_3+t_2+t_1)\mu(t_2+t_1)\},\mu(t_1)\}\{\mu(0),\rho_{\mathrm{eq}}\}. \end{aligned}$$

In a canonical ensemble one can apply Eq. 2.20:

$$R^{(3)}_{\mathrm{cl}}(t_3,t_2,t_1) = \int \mathrm{d}p \int \mathrm{d}q\ \{\{\mu(t_3+t_2+t_1),\mu(t_2+t_1)\},\mu(t_1)\}\beta\dot{\mu}(0)\rho_{\mathrm{eq}}$$

Repeating the same procedure again with the next Poisson bracket gives

$$R^{(3)}_{\mathrm{cl}}(t_3,t_2,t_1) = \int \mathrm{d}p \int \mathrm{d}q\ \beta\{\mu(t_3+t_2+t_1),\mu(t_2+t_1)\}(\{\mu(t_1),\dot{\mu}(0)\} - \beta\dot{\mu}(t_1)\dot{\mu}(0)\rho_{\mathrm{eq}}).$$

Now the Poisson brackets 2.14 are employed to give the final expression

$$\begin{aligned} R^{(3)}_{\mathrm{cl}}(t_3,t_2,t_1) &= \beta\langle\frac{\tilde{\partial}\mu(t_3+t_2+t_1)}{\partial\Gamma_{t_3+t_2+t_1}}\mathbf{M}(t_3+t_2+t_1,t_2+t_1)\mathbf{J}\frac{\partial\mu(t_2+t_1)}{\partial\Gamma_{t_2+t_1}} \\ &\quad\cdot\frac{\tilde{\partial}\mu(t_1)}{\partial\Gamma_{t_1}}\mathbf{M}(t_1,0)\mathbf{J}\frac{\partial\dot{\mu}(0)}{\partial\Gamma_0} \\ &\quad-\beta^2\frac{\tilde{\partial}\mu(t_3+t_2+t_1)}{\partial\Gamma_{t_3+t_2+t_1}}\mathbf{M}(t_3+t_2+t_1,t_2+t_1)\mathbf{J}\frac{\partial\mu(t_2+t_1)}{\partial\Gamma_{t_2+t_1}}\dot{\mu}(t_2)\dot{\mu}(t_1)\rangle \end{aligned} \tag{2.23}$$

Classical response functions were studied extensively for particles in Morse potential by Noid *et al.* [14] and Kryvohuz and Cao [17]. In both papers it is claimed that microcanonical trajectories (energy held constant) produce time-divergent results, whereas averaging over Boltzmann distributed initial conditions (thermal averaging) lets the response function decay and produces reasonable results. Noid *et al.* view this as an example of dephasing, i.e. the diverging terms from different trajectories cancel each other

out due to destructive interference. However, it was shown that the two-pulse photon echo $R_{\mathrm{cl}}^{(3)}(t,0,t)$ diverges linearly with time [14]. This can be understood as a rephasing of the classical trajectories, but is unphysical. Kryvohuz and Cao [17] argue that all **non-linear** response functions will diverge in some time directions in quasi-periodic systems ($f(x+\varphi) = f(x) + const$, with a period φ), due to the anharmonicity.

Wu and Cao [18] followed another approach. Instead of thermal averaging, they introduced a momentum uncertainty and sample the phase space in the uncertainty range. The quantum results are reproduced when setting the uncertainty equal to multiples of $\hbar$ depending on the order of the response function.

System	quasi-periodic	chaotic
stability matrix element	periodic	diverges
response from single trajectory	diverges	diverges?
ensamble averaged response	decays	decays

Table 2.1.: Behavior of stability matrix elements and response functions before and after averaging in chaotic and quasi-periodic systems.

The quantum commutator corresponds to the Moyal bracket, which in the first order of $\hbar$ is equal to the Poisson bracket. Kryvohuz and Cao [19] argue that the divergence of non-linear response functions in microcanonical ensemble thus results from neglecting higher order contributions. For a given order in the Moyal bracket the propagation reproduces the quantum result up to a crossover time, that depends inversely on anharmonicity of the system. Higher crossover times can be reached by taking more orders into the calculation.

However, in chaotic systems all response functions will always decay, if they are averaged correctly. Nevertheless, one should keep in mind that the stability matrix elements grow exponentially, producing huge numerical errors at long times.

2.4. 2d Spectra

To obtain 2d spectra the third-order response function is Fourier-transformed with respect to t_1 and t_3

$$R^{(3)}(\omega_3, t_2, \omega_1) = \int dt_1 dt_3 R^{(3)}(t_3, t_2, t_1) \exp(i\omega_1 t_1) \exp(i\omega_3 t_3)$$

and then plotted against ω_1 and ω_3 for a given population time t_2. Information about coupling of states and underlying dynamics of the molecule under study can easily be extracted now, as well as information on homogeneous and inhomogeneous broadening [4].

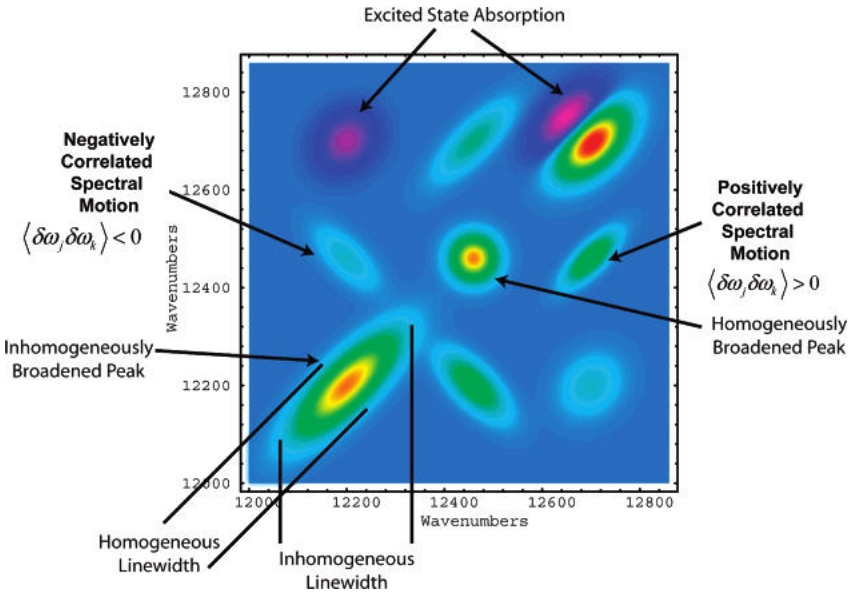

Figure 2.1.: A schematic 2d spectra taken from [10].

A schematic 2d spectrum for a fixed waiting time t_2 can be seen in Fig. 2.1. The excitation frequency is plotted on the abscissa, while the detection frequency is on the ordinate. For the diagonal peaks the excitation and detection frequencies are the same. The positive amplitude of the features is due to either ground state bleaching or stimulated emission. The upper right negative feature corresponds to an excited state absorption which is slightly red shifted compared to neighboring positive feature due to anharmonicity. Information about couplings and energy transfer can be gained from the so-called cross peaks.

3. Methods

How to treat the dynamics of molecular systems? There are many ways to model the dynamics, starting from a fully quantum mechanical treatment down to all classical propagation of nuclei in molecular mechanics. Quantum mechanical simulations are not only slow, they also scale exponentially in the degrees of freedom N, a fact that is referred to as 'curse of dimensionality'. Therefore it is very beneficial to use classical mechanics approaches, that scale at least as N^2 [1] or better, to treat a quantum problem.

3.1. Molecular Dynamics

In molecular dynamics simulations the nuclei are propagated in a potential according to Newton's equation of motion. But since the nuclei are quantum dynamical particles they obey the Schrödinger equation. In the following a very short derivation of molecular mechanics starting from the time-dependent Schrödinger equation is given. The molecular wave function $\left|\Psi(\vec{r},\vec{R},t)\right\rangle$ depends on the coordinates of electrons $\vec{r}$ and on the positions of the atoms, denoted by $\vec{R}$. It is the solution of the time-dependent Schrödinger equation

$$i\hbar\frac{\partial}{\partial t}\Psi(\vec{r},\vec{R},t) = H_{\text{mol}}\Psi(\vec{r},\vec{R},t)\ .$$

The Hamiltonian of a molecule H_{mol} has, setting spin-orbit coupling and relativistic effects aside, contributions from the kinetic energy of the nuclei T_{nuc} and of the electrons T_{el}, as well as Coulomb interactions between the nuclei V_{nuc}, the electrons V_{el} and between electrons and nuclei $V_{\text{nuc-el}}$

$$H_{\text{mol}} = T_{\text{nuc}} + V_{\text{nuc}} + T_{\text{el}} + V_{\text{el}} + V_{\text{el-nuc}}. \tag{3.1}$$

We define the electronic Hamiltonian as

$$H_{\text{el}} = T_{\text{el}} + V_{\text{el}} + V_{\text{el-nuc}}. \tag{3.2}$$

Due to the large mass difference between electron and nuclei $M_{\text{nuc}}/M_{\text{el}} > 10^3$ the electrons adapt almost instantaneously to a given nuclear configuration, so it is natural to separate the dynamics of the two. For fixed nuclei, we assume the solution of the time-independent Schrödinger for the electrons to be known for all electronic states a

$$H_{\text{el}} \left|\varphi_a(\vec{r}, \vec{R})\right\rangle = E_a(\vec{R}) \left|\varphi_a(\vec{r}, \vec{R})\right\rangle, \tag{3.3}$$

where here and in the following the time arguments are not shown. The total wave function $\Psi(\vec{r}, \vec{R})$ can then be expanded in the electron wave function $\varphi_a(\vec{r}, \vec{R})$ with the coefficients $\chi_a(\vec{R})$, the nuclear wave function

$$\left|\Psi(\vec{r}, \vec{R})\right\rangle = \sum_a \left|\chi_a(\vec{R})\right\rangle \left|\varphi_a(\vec{r}, \vec{R})\right\rangle \tag{3.4}$$

Following [12] the time-dependent Schrödinger equation for the nuclei wave function obeys

$$\left(T_{\text{nuc}} + V_{\text{nuc}}(\vec{R}) + E_a(\vec{R})\right) \chi_a(\vec{R}) + \sum_b \theta_{ab}\chi_b(\vec{R}) = i\hbar \frac{\partial}{\partial t}\chi_a(\vec{R}) \tag{3.5}$$

with the non-adiabatic coupling term θ_{ab} between different electronic states. The nuclei move according to Eq. 3.5 in the potential energy surface $V_{\text{nuc}} + E_a$, which is obtained by solving the time-independent Schrödinger Eq. 3.3. In the Born-Oppenheimer approximation the coupling θ_{ab} between states and θ_{aa} are set to zero, this implies that the movement of the nuclei does not change the electronic state. The next step is to approximate the nuclei as classical particles. Starting from the Born-Oppenheimer approximation the nuclear wave function χ_a is rewritten in the terms of an amplitude and a phase factor [20]

$$\chi_a(\vec{R}) = A_a(\vec{R}) \exp(\frac{i}{\hbar} S_a(\vec{R})).$$

This ansatz leads to, the classic limit taken, a Newtonian equation of motion for the nuclei

$$M\ddot{\vec{R}} = -\nabla V_a^{\text{BO}}(\vec{R}) \tag{3.6}$$

with the mass of the nucleus M. The so-called Born-Oppenheimer potential $V_a^{\mathrm{BO}}(\vec{R}) = E_a(\vec{R}) + V_{nuc}(\vec{R})$ for each electronic state a has to be calculated by solving the time-independent Schrödinger Eq. 3.3 for the electrons. In this so-called Born-Oppenheimer molecular dynamics the nuclear move according to classical mechanics, but the electrons still according to quantum mechanics [20].

The computation of the forces on the fly by the evaluation of the Born-Oppenheimer potential $V_a^{\mathrm{BO}}(\vec{R})$ is computationally expensive. Since the focus is on the dynamics of the nuclei only, the next simplification is to pre-compute the potential energy surface and parametrize the potential. Electrons are then no longer treated explicitly. The nuclei move according to

$$\vec{F} = M\ddot{\vec{R}} = -\nabla V(\vec{R}) \tag{3.7}$$

with the potential

$$V(\vec{R}) = V_{\mathrm{bond}}(\vec{R}) + V_{\mathrm{angle}}(\vec{R}) + V_{\mathrm{dihedrals}}(\vec{R}) + V_{\mathrm{Coulomb}}(\vec{R}) + V_{\mathrm{vdW}}(\vec{R}) \tag{3.8}$$

consisting of bonding and non-bonding interactions. Usually the bonding part describes 1-2, 1-3 and 1-4 interactions, that is bonds, angles and dihedrals. The bonds and angles are commonly described by harmonic potentials

$$V_{\mathrm{bond}}(R) = \sum_{\mathrm{bonds}} k_R(R - R_0)^2 \quad \text{and} \quad \mathrm{V}_{\mathrm{angle}}(\theta) = \sum_{\mathrm{angles}} \mathrm{k}_\theta(\theta - \theta_0)^2$$

where R_0 and θ_0 are the equilibrium distance and angle, respectively, and k_i are corresponding force constants. The non-bonded interactions consist of a van der Waals term modeled by the Lennard-Jones potential and the Coulomb potential

$$V_{\mathrm{nonbonded}} = \sum_{i>j} E_{ij} \left(\left(\frac{\sigma_{ij}}{R_{ij}} \right)^{12} - \left(\frac{\sigma_{ij}}{R_{ij}} \right)^{6} \right) + \frac{q_i q_j e^2}{4\pi\epsilon_0 R_{ij}}.$$

with the partial charges q_i, the elementary charge e, the vacuum permittivity ϵ_0 and the Lennard-Jones interaction range σ_{ij} and the energy well depth E_{ij}. The complete set of parameters specifying the potentials is called a force field.

3.1.1. Thermostats and Ensembles

Newton's equations of motion are intrinsically microcanonical (NVE), that is the total energy is conserved. Since the response functions need to be averaged over Boltzmann distributed initial conditions the trajectories must be sampled from the canonical distribution (NVT), i.e. the system can exchange energy with a heat bath, thus having a defined temperature T. The equations of motion must be modified to produce canonical ensemble, which is done by employing so-called thermostats. Historically the simplest approach is to rescale velocities $\vec{v}$ to the desired temperature via the relation of the equipartition theorem

$$\frac{3}{2}Nk_{\mathrm{B}}T = \sum_i \frac{1}{2}m_i\vec{v}_i^2, \tag{3.9}$$

which links the average kinetic energy to the temperature, with i the index of the degrees of freedom. While this rescaling of velocities can be used to control the temperature, it does not produce the canonical ensemble. The correct ensemble can be produced by a Nosé-Hoover thermostat. Martyna *et al.* [21] have shown analytically that this scheme produces a canonical ensemble automatically. In this approach an additional time-dependent 'friction' term $\dot{\zeta}(t)$ (although it can be positive and negative) is introduced into the equations of motion

$$M\ddot{\vec{R}} = \vec{F} - \dot{\zeta}(t)m\dot{\vec{R}} \; . \tag{3.10}$$

The additional term $\zeta(t)$ describes the coupling of the system to a virtual heat bath with the mass Q.

$$\ddot{\zeta}(t) = \frac{1}{Q}(\sum_i m_i\vec{v}_i^2 - 3Nk_{\mathrm{B}}T) \; .$$

The force acting on the bath variable $\zeta(t)$ is proportional to the difference in instantaneous kinetic energy of the system and the average kinetic energy at the desired temperature. The feedback of $\dot{\zeta}$ through Eq. 3.10 therefore brings the system to the desired temperature T. In the so-called massive Nosé-Hoover scheme each degree of freedom is coupled to a separate bath, which is especially useful if the system consists of heavy and light atoms. Additionally in cases where the systems is not ergodic, chains of thermostats are used to ensure that the canonical ensemble is produced [21]. In a chain the thermostat coupled to the system is thermostated by another thermostat, which is coupled to the next thermostat, and so on.

3.2. Integrators

To calculate the classical response functions 2.16 and 2.24 one needs the time evolution of the stability matrix $\mathbf{M}$, which is calculated from classical trajectories. A particle is propagated by Newton's equations and simultaneously the matrix elements are computed. The evolution of the stability matrix in time is governed by the Hessian of the Hamiltonian of the system according to

$$\frac{\partial \mathbf{M}(t,t')}{\partial t} = \begin{pmatrix} 0 & \frac{\partial}{\partial p_t}\frac{\tilde{\partial}}{\partial p_t}H_t \\ -\frac{\partial}{\partial q_t}\frac{\tilde{\partial}}{\partial q_t}H_t & 0 \end{pmatrix} \mathbf{M}(t,t'). \tag{3.11}$$

Two integration steps are performed, namely the integration of Newton's equation and the stability matrix equation of motion 3.11. The algorithms chosen to solve the two equations of motion have to fulfill three requirements. They should be simple, simplectic and efficient. In principle the same integrator can be used to propagate the system and the stability matrix. Because the Hessian calculation is computationally expansive in ab initio MD simulation, and in QM/MM, it would be good to have an algorithm that evaluates the Hessian matrix less often. Algorithms like Runge-Kutta in which many evaluations per time step are made, are therefore inefficient. A good standard choice is a Verlet integrator and I will present a method developed by Yun-an Yan [31], the **matrix exponential**.

The Velocity Verlet, which is similar to the leap frog algorithm, but with the advantage that velocities and positions are evaluated at the same time, works as follows, first a half time step in the velocities is made followed by full step of the positions and a call of the forces before the second half step of velocities is made

$$\begin{aligned} \dot{r}(t+\frac{\Delta t}{2}) &= \dot{r}(t) + \frac{1}{2}\ddot{r}(t)\Delta t \\ r(t+\Delta t) &= r(t) + \dot{r}(t)\Delta t + \frac{1}{2}\ddot{r}\Delta t^2 \\ \ddot{r}(t+\Delta t) &= -\frac{1}{m}\nabla V(r) \\ \dot{r}(t+\Delta t) &= \dot{r}(t+\frac{1}{2}\Delta t) + \frac{1}{2}\ddot{r}(t+\Delta t)\Delta t \ . \end{aligned}$$

Another possible integrator for the stability matrix equation of motion, developed by Yun-an Yan [31], works by integrating Eq. 3.11

$$\mathbf{M}(t,t_0) = \mathcal{T}\exp\left\{\int_{t_0}^{t} dt_1 \begin{pmatrix} 0 & \frac{\partial}{\partial \vec{p}_t}\frac{\tilde{\partial}}{\partial \vec{p}_t}H_t \\ -\frac{\partial}{\partial \vec{q}_t}\frac{\tilde{\partial}}{\partial \vec{q}_t}H_t & 0 \end{pmatrix}\right\} \tag{3.12}$$

and taking the short-time approximation

$$\mathbf{M}(t,t_0) \quad = \quad \exp\left\{\Delta t \begin{pmatrix} 0 & \frac{\partial}{\partial \vec{p}_t}\frac{\tilde{\partial}}{\partial \vec{p}_t}H_t \\ -\frac{\partial}{\partial \vec{q}_t}\frac{\tilde{\partial}}{\partial \vec{q}_t}H_t & 0 \end{pmatrix}\right\}. \tag{3.13}$$

Together with the chain rule

$$\mathbf{M}(t,t') = \mathbf{M}(t,\tilde{t})\mathbf{M}(\tilde{t},t'). \tag{3.14}$$

the whole stability matrix trajectory can be reconstructed from the short time approximations. In some cases the computation of the Hessian trajectory is expensive. Therefore it is of advantage if many stability matrix trajectories can be computed based on a single Hessian trajectory. Stability matrix trajectories are started with an time offset dt between each other and then propagated along the same Hessian trajectory up to the total simulation time, see Fig. 3.1. The response function $R^{(1)}(t)$ computed that way is the sum of the response functions computed from just a single stability matrix trajectory $R^{(1)}(t,\tau)$ with starting time τ

$$R^{(1)}(t) = \frac{1}{N}\sum_{n=0}^{N} R^{(1)}(t+ndt, ndt),$$

N being the number of parallel stability matrix trajectories. Naturally the average over the canonical ensemble still has to be taken. An analogous scheme can be applied for the calculation of non-linear response function, not shown. It should be noted that in the model systems considered the computational advantage is small, because the Hessian can be calculated analytically.

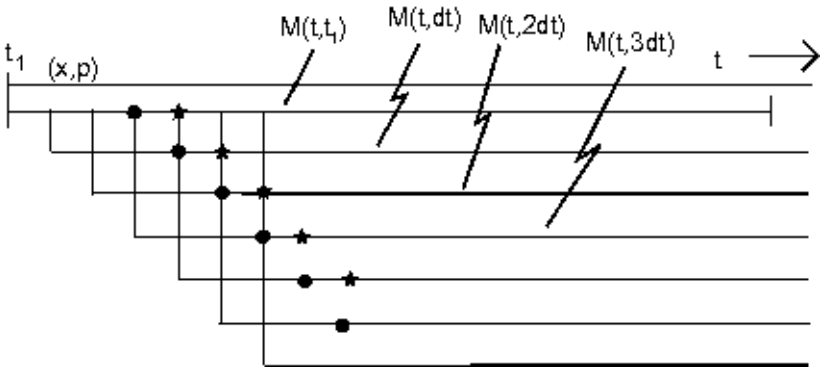

Figure 3.1.: Efficient algorithm scheme for linear response. The upper line is the phase space trajectory. All other lines symbolize stability matrix trajectories. They are started with an offset of dt. All marked stars then contribute to the response $R^{(1)}(t = 4dt)$

3.3. Model Systems

To test the classical response function formalism two model systems are used. A 1d Morse potential, common in molecular physics to describe bonds, is used as an example for a quasi-periodic system. The potential has a dissociation energy D at the equilibrium distance r_0 and anharmonicity α

$$V_M(r) = D\Big(1 - \exp\left(-\alpha\left(r - r_0\right)\right)\Big)^2. \tag{3.15}$$

The energy levels for the quantum number ν are analytically calculated by

$$E_\nu = \hbar\omega_0(\nu + 1/2) - \frac{\hbar^2\omega_0^2}{4D}(\nu + 1/2)^2,$$

with constants ω_0 and D that are related to the parameters of the potential. For increasing quantum numbers, the energy difference between levels is decreasing.

Since its introduction in 1964 to describe chaotic stellar motion, the Hénon Heiles potential has gained a lot of interest in very different contexts [35]. This is due to the diverse behavior appearing in Hénon Heiles systems. In a general form the potential reads [22]

$$V(x, y) = \lambda_1 x^2 + \lambda_2 y^2 + \lambda_3 x^2 y - \lambda_4 y^3 \ . \tag{3.16}$$

For most choices of λ_i the Hamiltonian is not integrable, i.e. it produces chaotic dynamics. The choice is $\lambda_4 = 1/3$, $\lambda_3 = 1$ and $\lambda_2 = \lambda_1 = 1/2$, which produces a non-integrable system [22]

$$V(x,y) = \frac{1}{2}\left(x^2 + y^2\right) + x^2 y - \frac{1}{3}y^3 \ . \tag{3.17}$$

The potential forms a triangular-like shaped well with three saddle points, $P_1(x=0,y=1)$, $P_2(\sqrt{(3/2)}, -1/2)$ and $P_3(-\sqrt{(3/2)}, -1/2)$ [22]. For our parameter choice a particle can escape from the well through the saddle points, if its energy is above a threshold energy $E_{\text{th}} = 1/6$. Below the threshold energy E_{th} the particle stays bound, but can behave qualitatively different. For small energies the motion is regular/deterministic/integrable. Above $E_{\text{c}} = 1/12$ parts of the trajectory become chaotic until it is fully chaotic at E_{th} [23]. This regime change is very important in the context of the response function behavior.

3.4. Normal Modes

A useful tool to analyze bands in spectra is the normal mode analysis (NMA). Conventional normal mode analysis is performed on a energy minimized structure, that is at zero kelvin and with only one possible molecular conformation. 'However, finite temperature effects, such as shifting and broadening of bands, due to the fluctuating structure of the molecule or its solvent environment in condensed phase are beyond the scope of traditional NMA methods' [24].

A calculation of normal modes from MD trajectories would ensure a proper sampling of the free energy surface and therefore include finite temperature effects. Mathias and Baer [24] established a way to compute 'dynamic normal modes' directly from MD trajectories and implemented it in the Normcor code. The normal modes are first constructed from guessed initial mass-weighted Cartesians. In an iterative scheme the correlation between the normal modes is minimized with a strategy based on the Jacobi diagonalization. To measure the correlation, a function of the tensorial formulation of the vibrational density of states is minimized. The equipartition theorem, which has caused trouble in similar approaches, is not used. Furthermore it is possible to use different reference structures to compute normal modes [25].

3.5. Computational Details

In the following the information on all performed computations is summarized. Molecular mechanics simulations are performed using Gromacs 4.02 and the force field developed by [26]. A general force field to treat ionic liquids is not available, as it is the case for example for simulations of biomolecules with the AMBER parameters [27]. Here, the [C_2mim] [NTf_2] is modeled by a force field developed by Köddermann *et al.* [26] specifically developed to describe imidazolium based cations with varying chain length and [NTf2] anions. It originates from a force field by Lopes and coworkers [28], who refined OPLS parameters using ab initio calculations for torsion profiles. Ködderman *et al.* then fit the Lopes' Van der Waals parameters to experimental data from diffusion experiments and density measurements, to get a more accurate description of diffusion and heat of vaporization.

The starting geometry of [C_2mim] [NTf_2] is taken from a Gaussian [36] geometry optimization calculation with B3LYP functional and a 6-31+G(d) (6D, 7F) basis on the DFT level of theory. Since the C-H stretches in the force field are constrained, harmonic bonds parameters are taken from OPLS-aa force field for alkanes. Using Gaussian with the same basis set and functional, energy profiles along the three bonds in gas phase are computed. The result is fitted to a Morse potential 3.15 using Gnuplot 4.0, see Tab. 3.1. To calculate dynamic normal modes 10 microcanonical trajectories with $dt = 0.25$ each 10 ps long are produced with output of the positions every 4 steps. The Normcor code [24] is used to calculate normal modes. The ab initio molecular

	r_0 [Å]	D [kJ/mol]	α [Å^{-1}]
C(2)-H	1.0854	$0.587 \cdot 10^3$	1.758
C(4)-H	1.0851	$0.591 \cdot 10^3$	1.753
C(5)-H	1.0848	$0.591 \cdot 10^3$	1.754

Table 3.1.: Morse parameters for the three C-H stretches investigated obtained from a fit of gas phase results using the Gaussian program.

dynamics were computed by Terachem [32] with 6-31+gs basis and BYLP functional. One microcanonical trajectory with 10 ps length and $dt = 0.33$fs was compute and analyzed with Normcor, as well as a Langevin dynamics trajectory with 7.5 ps length and $dt = 0.25$fs.

We study a cation in the gas phase, a monomer in gas phase, and bulk, which consists of 686 molecules in total. It is assumed that the partial charge model works, therefore charges of the atoms remain unchanged along the dynamics and the dipole moment can then be written as

$$\vec{\mu}(t) = \sum_j q_j \vec{r}_j(t). \tag{3.18}$$

In 2d and higher dimensional systems it is helpful to set the dipole moment linear to internal coordinates to calculate the response i.e. to set $\vec{\mu}(t) = c_x x\vec{e_x} + c_y y\vec{e_y} + .. .$ With $c_i = 1$ we get

$$\begin{aligned} R^{(1)}(t) &= -\left\langle \sum_{ij} \mathbf{M}_{ij}^{\mathrm{QP}}(t,0) \right\rangle \\ R^{(3)}(t_3,t_2,t_1) &= \frac{\beta}{m} \left\langle \left(\sum_{ij} \mathbf{M}_{ij}^{\mathrm{QP}}(t_3+t_2+t_1, t_2+t_1) \right) \left(\sum_{ij} \mathbf{M}_{ij}^{\mathrm{QQ}}(t_1,0) \right) \right\rangle \\ &- \left(\frac{\beta}{m}\right)^2 \left\langle \left(\sum_{ij} \mathbf{M}_{ij}^{\mathrm{QP}}(t_3+t_2+t_1, t_2+t_1) \right) \left(\sum_i p_i(t_1) \right) \left(\sum_i p_i(0) \right) \right\rangle, \end{aligned} \tag{3.19}$$

with

$$\mathbf{M}^{\mathrm{QP}}(t_1,t_2) = \frac{\partial q(t_1)}{\partial p(t_2)} \ .$$

These are the formulas used to calculate classical response functions in the following.

4. Results

4.1. Model Systems

Before going to a real system the response function behavior is investigated for small model systems. The focus is on convergence properties and the reliability of the classical response functions.

4.1.1. Stability Matrix

As discussed in [14] the main ingredient to calculate (non-) linear response functions 3.20 is the stability matrix. The behavior of stability matrices is different in quasi-periodic and chaotic systems, see Tab. 2.1 and chapter 2 for the discussion, and will be considered for separate model systems, namely the 1d Morse potential and a 2d Hénon Heiles potential for quasi-periodic and chaotic motion, correspondingly. To illustrate, the time evolution of a stability matrix element is shown in Fig. 4.1 and 4.2 for quasi-periodic and chaotic motion. In the former case the stability matrix elements are oscillating with the same frequency as the particle in the potential, as is expected in a quasi-periodic system, but with a surprisingly high amplitude, as all variables and constants are in intrinsic units with a values around one. In the latter case the considered element diverges exponentially. The question is if and how these diverging numbers cause problems during the propagation and it will be tested in detail in the following. No problems are expected concerning the oscillating stability matrix elements in Morse, thus only the Hénon Heiles potential is investigated.

To deduce how the divergence in chaotic systems influences the numerical stability of the stability matrix propagation various numerical algorithms are applied to solve

Eq. 3.11. To quantify the computational stability of the system the condition

$$\det\Big(\mathbf{M}(\mathrm{t},\mathrm{t}')\Big) = 1 \tag{4.1}$$

is employed, which must holds because phase space volume has to be conserved.

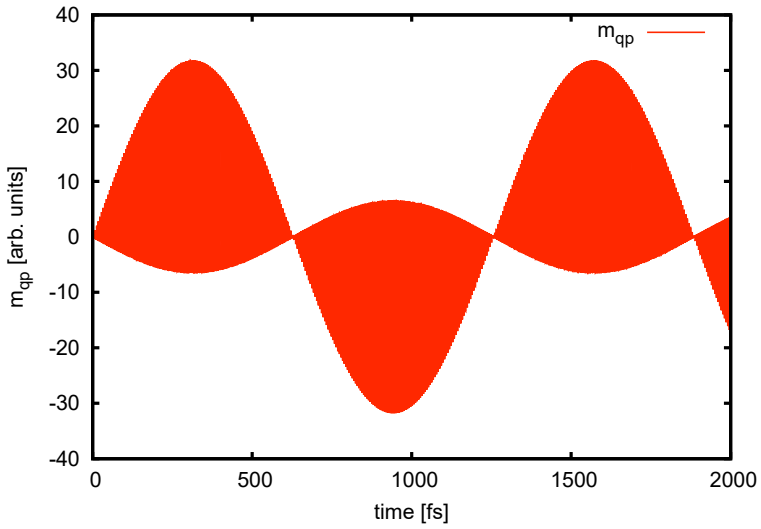

Figure 4.1.: Morse potential: Time evolution of a representative stability matrix element.

In Fig. 4.3 time evolution a representative stability matrix element in Hénon Heiles potential is shown as obtained from the matrix exponential propagation method using different time steps. Interestingly the longest time steps (1fs) produces the best results, whereas increasing the time step further (2 fs) leads to an immediate divergence, not shown. The same time steps are used with the leap-frog algorithm, see Fig. 4.4. Decreasing the time step from 1 fs down to 0.1 fs increases the stability of the determinant, but the improvement is small. The optimal time step for the matrix exponential scheme turns out to be 1 fs while leap-frog produces the best results with $dt = 0.1$ fs time steps. A Runge-Kutta forth order integrator (Fig. 4.5) produces a little worse results than leap-frog at $dt = 0.1$ fs and fails to keep the determinant stable at $dt = 0.2$ fs, but the results improve for $dt = 0.01$. However, a disadvantage of the Runge-Kutta fourth order is the multiple evaluation of the Hessian per time step. Naively one would assume that a smaller time step decreases the total error of the simulation. While a smaller time step reduces the error per step it also implies that more steps need to be made to reach the same total simulation time. More steps might increase the total error of

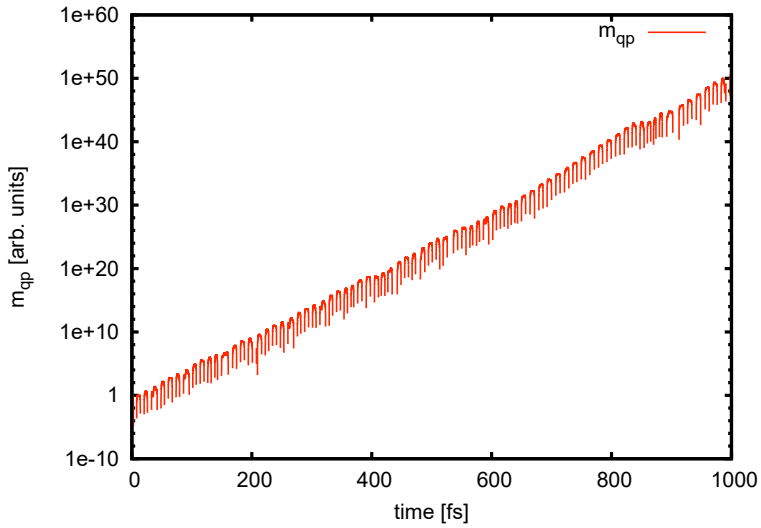

Figure 4.2.: Hénon Heiles potential: Time evolution of a representative stability matrix element, note the logscale.

the simulation, because the errors per step accumulate. Then an error reduction per step via time step reduction might be outweighed by the necessary increase of total step number. It might be this complex interplay between the two effects that causes these somewhat counter-intuitive results in some of the presented data, such as the increase of the stable trajectory length for a decrease in time step using the matrix exponential method.

Now after the propagation algorithms have been investigated, the calculation of the determinant is going to be analyzed. In Fig. 4.6 the determinant computed by a matrix diagonalization algorithm is compared to the direct determinant calculation. Furthermore to check the program, a velocity Verlet algorithm was programmed to propagate the system and the stability matrix and calculated the determinant directly, see Fig. 4.6. Both direct determinant calculations yield the same results, but the matrix diagonalization scheme works slightly better. This shows how sensitive the stability matrix propagation is to the numerics chosen.

Finally, in Fig. 4.7 the impact of the floating point precision is investigated. As expected higher precision produces a stable determinant equal to unity for longer times. Exponential growth of the stability matrix elements means that the number of digits needed to represent the stability matrix elements increases linearly with time. As can

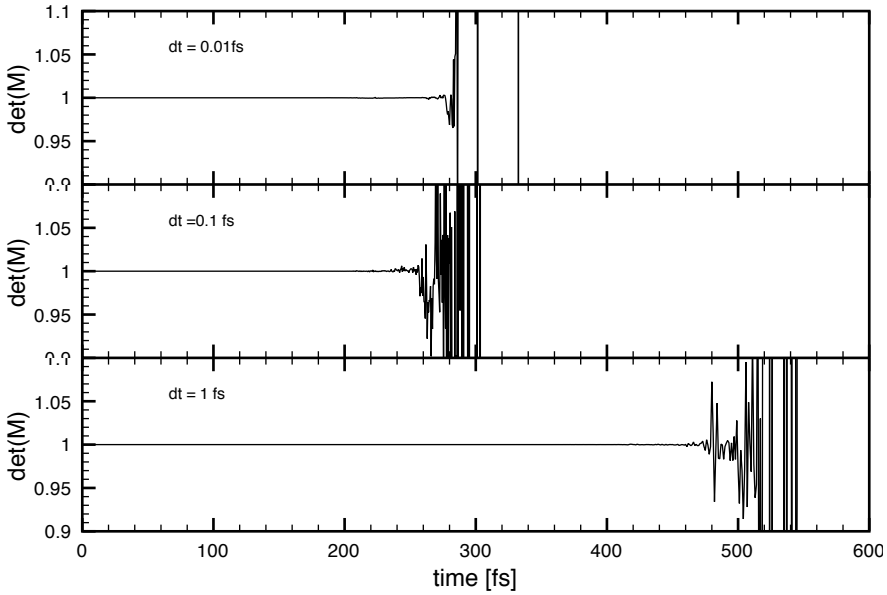

Figure 4.3.: Hénon Heiles potential: Stability of the matrix exponential method with respect to different time steps (increasing from top to bottom). Using larger time steps (for example 2 fs) results in immediate divergence.

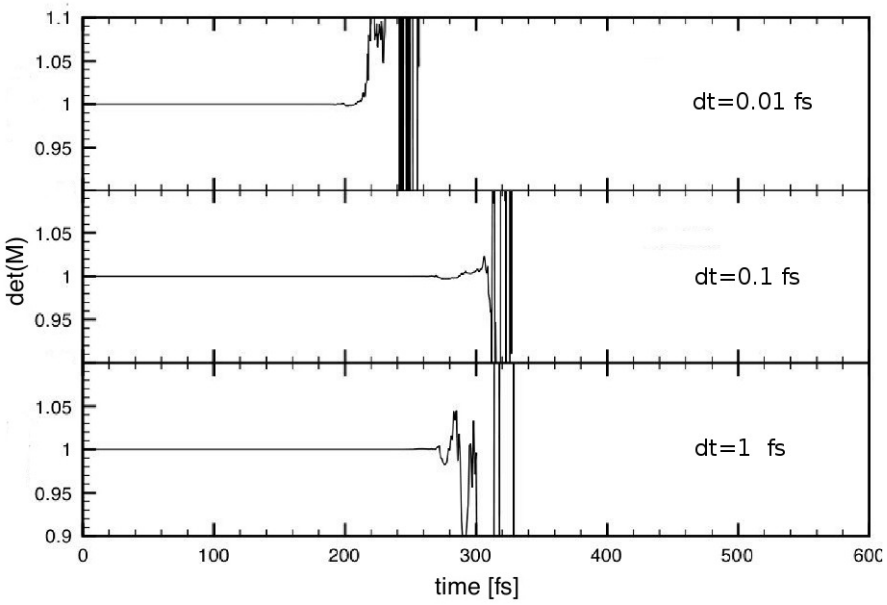

Figure 4.4.: Hénon Heiles potential: Stability of the leap-frog method with respect to different time steps (increasing from top to bottom).

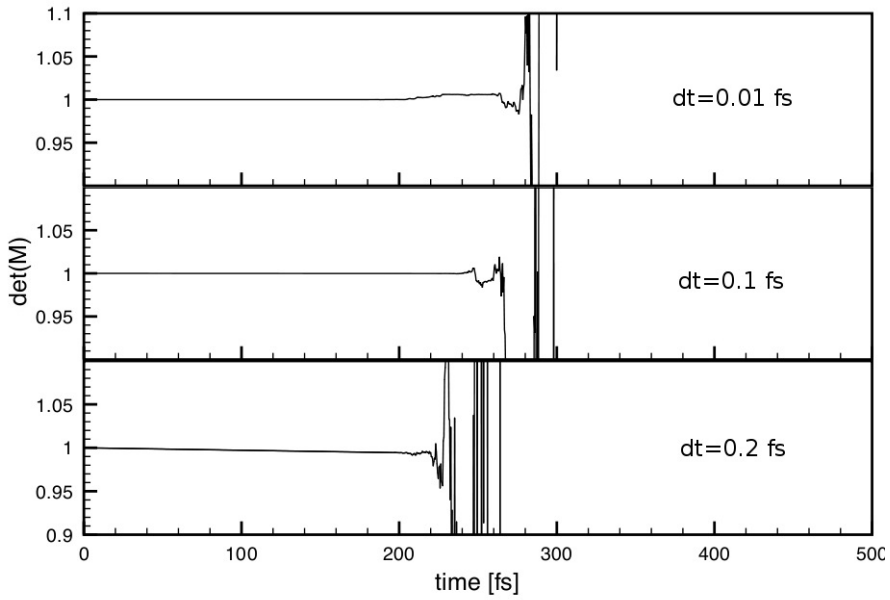

Figure 4.5.: Hénon Heiles potential: Stability of the Runge-Kutta method with respect to different time steps (increasing from top to bottom). The result for $dt = 0.2$ is drifting linearly already for small times.

be seen from Fig. 4.2 doubling the time roughly doubles the needed number of digits. At $t = 120$fs the matrix element has a value in the order of 10^7 and at $t = 240$fs approximately 10^{14}, which corresponds to the length of the stable stability matrix trajectories for single and double precision, respectively. The improvement of using long double, a 80 bit variable, is not as big as expected. This shows that the theory is limited by a lack of numerical precision.

To summarize, it is the exponential divergence that is at the root of all described numerical problems. Nonetheless, the velocity Verlet and matrix exponential methods produce good results, the latter even for comparably large time steps. Runge-Kutta fourth order does not give satisfactory results. In general the dynamics are very sensitive to the chosen numerical method, as could be seen from the determinant calculation.

4.1.2. Response Functions in Quasi-Periodic Systems: Morse Potential

In the previous section various integrators were investigated and the velocity Verlet algorithm was chosen as the method to propagate the stability matrix, as it combines

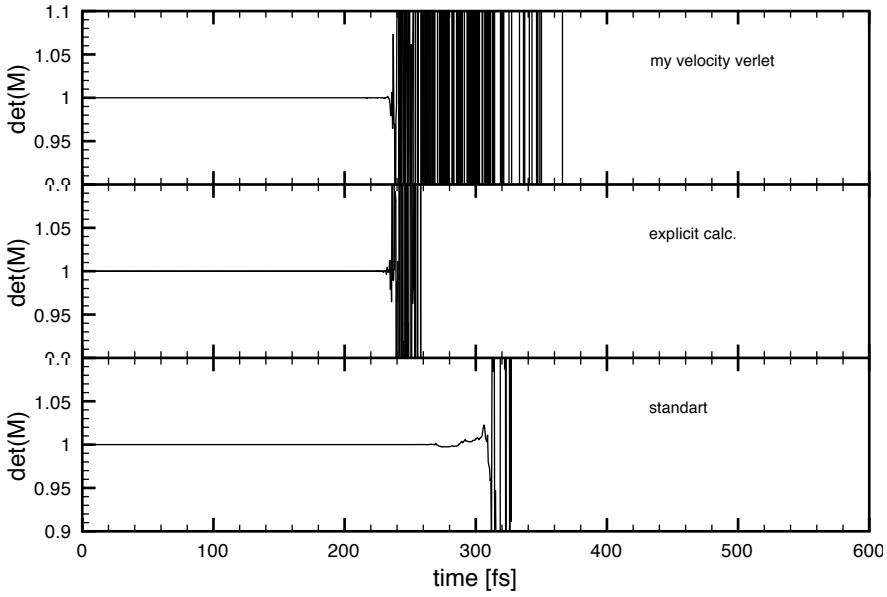

Figure 4.6.: Hénon Heiles potential: The leap-frog method with direct determinant calculation and a matrix diagonalization method are compared to a velocity Verlet with direct determinant calculation. Time step is = 0.1 fs in all simulations.

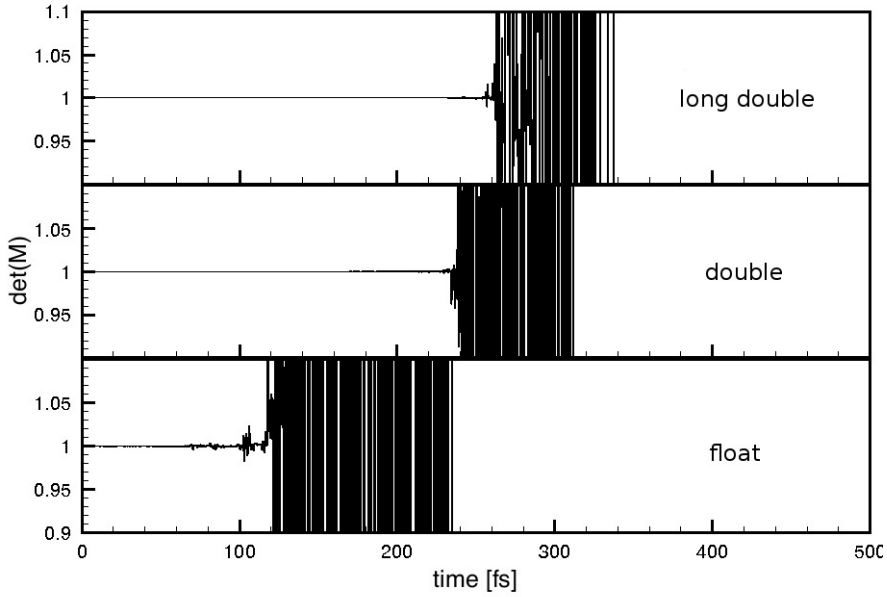

Figure 4.7.: Hénon Heiles potential: Comparison of different floating points, precision increasing from bottom to top, using velocity Verlet method, a time step $dt = 0.1$ fs and direct determinant calculation. The double precision result are the same as the top panel in Fig. 4.6

simplicity and stable propagation. Matrix exponential method produces longer reliable trajectories at $dt = 1$fs, but this is a too high time step for investigating dynamics of Hydrogen atoms, which will be the case in ionic liquids. Classical response function behavior in Morse potential were discussed in Refs. [14] and [19] already. The authors claim, as discussed in Chapter 2, that the response function of a single trajectory diverges in a Morse potential and decays after thermal averaging. The used Morse potential parameters in the following are: potential depth is set $D = 1$, as is the anharmonicity α and temperature is set in accordance with Ref. [14] to $\beta = 1/k_{\mathrm{B}}T = 12.8$. The linear classical response $R^{(1)}(t)$ is the Boltzmann average of the upper right stability matrix element $\partial q_t/\partial p_{t'}$, see Eq. 3.20. This implies that the response from just one trajectory is oscillating, just like the stability matrix elements in Fig. 4.1. The response function averaged over the microcanonical ensemble, where all initial conditions have the same energy, behaves similar to the response function from a single trajectory.

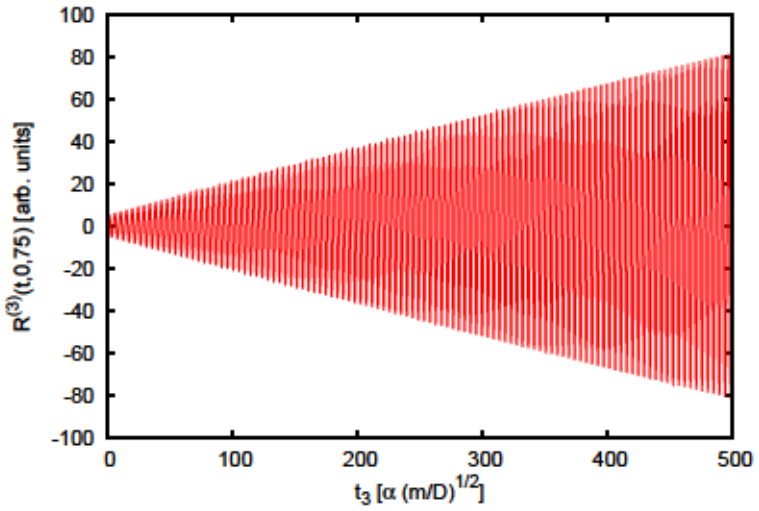

Figure 4.8.: Morse potential: Linear response calculated from a single trajectory

In the literature it is further stated that a Boltzmann average produces decaying response functions. The averaging via Eq. 3.20 produces more and more decaying response function, as can be seen in Fig. 4.10, where the ensemble is increased from a hundred to ten thousand trajectories sampled from Boltzmann distributed initial conditions. The linear response converges for an ensemble of one million trajectories as is shown in Fig. 4.10. As the response function should, it decays to zero but the convergence puts high demands on the statistics required. Noid *et al.* explain the resulting decay with the

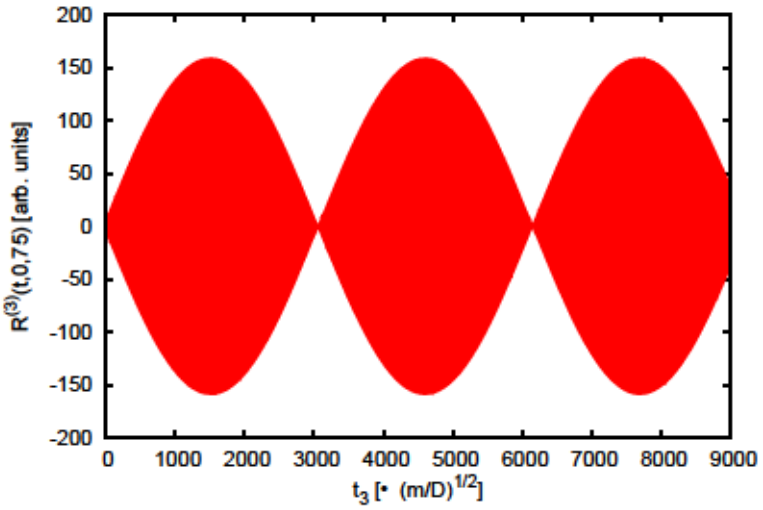

Figure 4.9.: Morse potential: Non-linear response calculated from a single trajectory

dephasing of the trajectories in the canonical ensemble and the destructive interference between the 'dephased' trajectories. The 'usual' way of calculating linear response via Eq. 2.17 produces qualitatively the same result, but shifted in phase, since the response function starts at time $t = 0$ with $R(t = 0) = 0$ whereas the correlation function at $C(t = 0) = 1$.

The non-linear response $R^{(3)}(t_3, 0, t_1)$ for a fixed $t_1 = 75$ calculated from just one trajectory is shown in Fig. 4.8. This figure coincides with Fig. 1 in [14] where it is claimed that $R^{(3)}(t, 0, 75)$ diverges. Nonetheless, when the simulation time is increased the response seems to be oscillating, see Fig. 4.9. The averaged non-linear response function also stays finite and decays for longer times, as shown in Fig. 4.11 for one million trajectories. For a coherence time t_1 between the two interaction times the signal has a peak after the interval $t_3 \approx t_1$. The stability matrix elements are rephasing after the time $t_1 = t_3$ to produce a signal. The 'weighted sum of divergent contributions from each energy produces a result that does not diverge in time' [14]. The peak is a little shifted to longer times because of the anharmonicity of the Morse potential.

Up to now the non-linear response function's only time argument was t_3. The response function $R^{(3)}(t, 0, t)$ shown in Fig. 4.12 is linearly diverging in t. As one point of $R^{(3)}(t_3, 0, t_1)$ always coincides with a point in $R^{(3)}(t, 0, t)$ by construction, namely the point with $t_1 = t_3$, this means the amplitude of the echo signal grows with the coher-

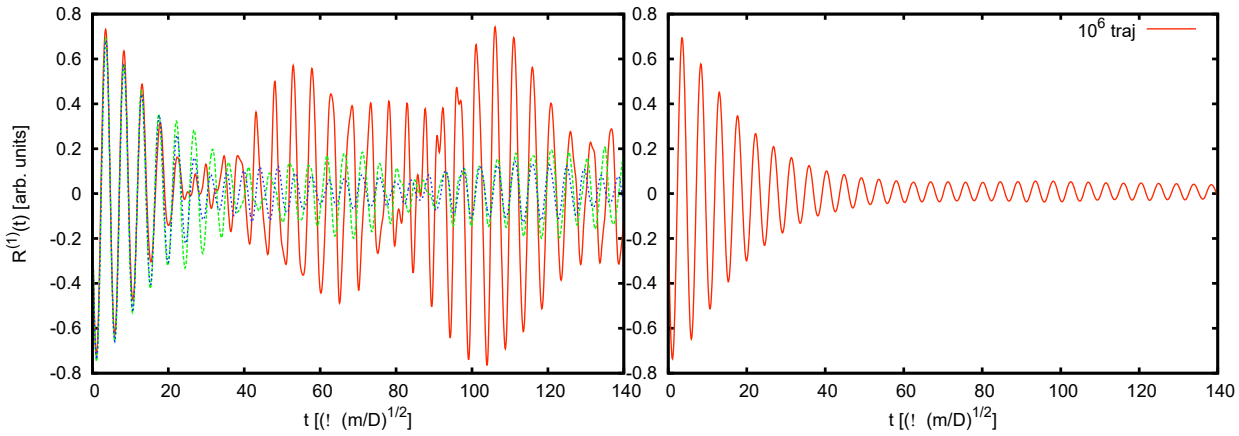

Figure 4.10.: Morse potential: linear classical response function calculated from 10^2, 10^3 and 10^4 trajectories (left) and 10^6 trajectories (right).

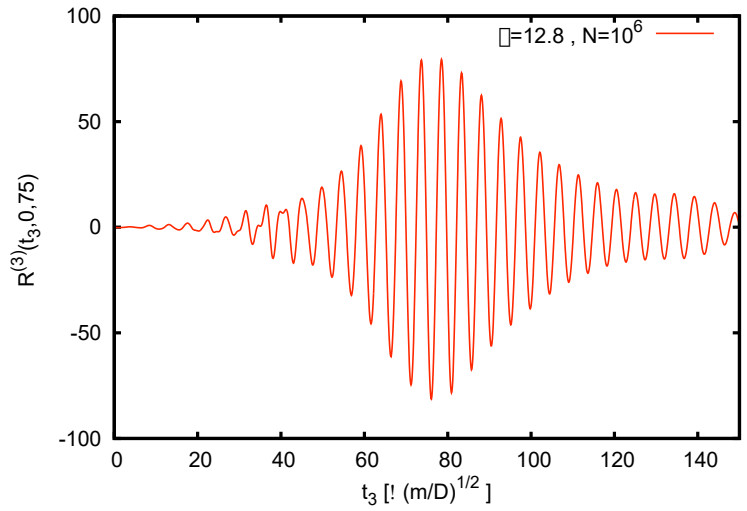

Figure 4.11.: Morse potential: non-linear classical response function calculated from one million trajectories

ence time t_1, which is not physical! Instead a longer coherence time between the pulses should decrease the amplitude of the signal. While in the $R^{(3)}(t, 0, 75)$ case the oscillating matrix elements deconstructively interfere with the ones from other trajectories, the interference in the echo setup is constructive in $t_1 + t_3$.

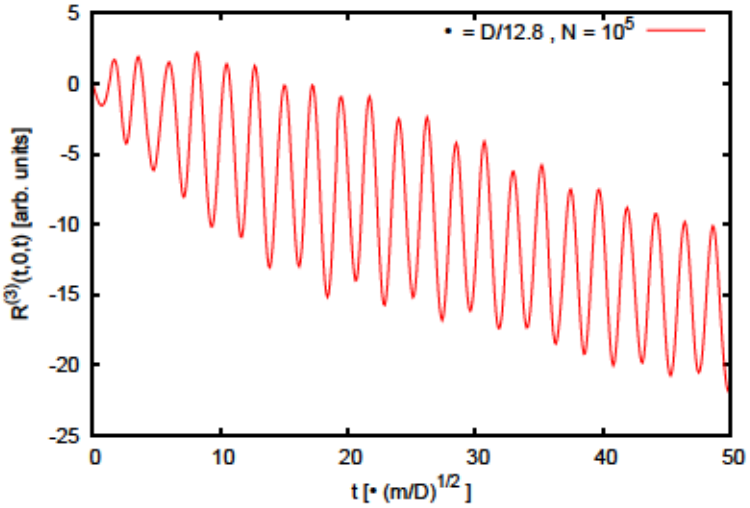

Figure 4.12.: Morse potential: response function in the echo setup $R(t,0,t)$ ensemble averaged over 10^5 trafectories. The response diverges linearly in t!

The divergence seen in $R(t,0,t)$ can also be seen in the 2d plot of the non-linear response function in Fig. 4.13. The classical response increases in $t_1 + t_3$ and makes a Fourier transformation impossible. This divergence is not the result of numerical instability due to diverging matrix elements. This is a feature of the classical limit in the case of quasi-periodic systems.

To summarize, the classical linear response functions of a particle in a Morse potential decays if averaged extensively over a canonical ensemble. An averaging over microcanonical ensemble (not shown) or the response function of just a single trajectory is a finite oscillating function in time. This is in contrast to the commonly accepted opinion [14], that the response function are diverging in a microcanonical ensemble. The non-linear response function for a fixed coherence time t_1 and population time $t_2 = 0$ analogously stays finite and decays out long times after averaging over the canonical ensemble. Furthermore the two pulse echo response function $R^{(3)}(t,0,t)$ diverges linearly, making it impossible to calculate a spectrum, and in particular the 2d spectrum.

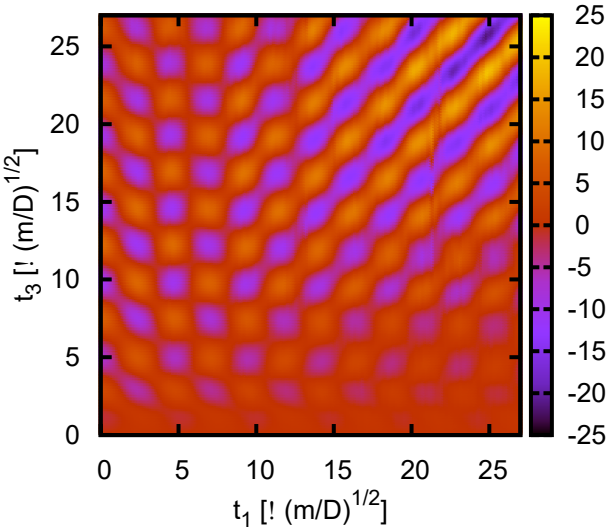

Figure 4.13.: Morse potential: 2d visualization of the non-linear response with population time zero and $\beta = 12.8$.

4.1.3. Response Functions in Chaotic Systems: Hénon Heiles Potential

Next investigations are performed for a 2d model system given as the Hénon Heiles potential, which features both quasi-periodic and chaotic regimes as discussed in Chapter 3.

The individual stability matrix elements in the chaotic regime are diverging because in chaotic systems neighboring trajectories diverge exponentially. But nonetheless the linear response function decays, see Fig. 4.14, as in quasi-periodic systems. The assumed problem arising from the exponential divergence of the stability matrices does not play a role, because the response function is heavily averaged and the response function stays finite for a long enough time, making it possible to calculate a spectrum.

The Fourier transform of the linear response function is shown for various temperatures $\beta = 1/k_{\mathrm{B}}T$ in Fig. 4.15. The harmonic frequency ω_0 is equal to unity, because the harmonic prefactor $m\omega^2/2$ in the Hénon Heiles potential 3.16 is set to 1/2 and the mass to 1. For low temperatures, $\beta = 80$, only the quasi-periodic region is probed and only one peak at the harmonic frequency $\omega = 1$ is visible. High temperatures mean high average kinetic energies and thus more particles will have an energy higher than the threshold energy 1/12 above which trajectories become chaotic, see section 3.3. The chaotic region is more anharmonic and the peak is shifted a little to smaller frequencies and an additional peak is visible at $\omega = 0.97$ for $\beta = 30$. Using higher temperatures is problematic because trajectories with an energy above 1/6 can escape the potential well and are therefore removed from the statistics.

Analogously to the linear response the non-linear response function produce reasonable results after the thermal averaging. Exemplarily the non-linear response $R^{(3)}(t, 0, 25)$ is plotted in Fig. 4.16. At $\beta = 30$ the response function eventually grows exponentially at long times, but the response produced at short times appears to be reasonable. Depending on the amount of averaged trajectories the exponential divergence of the response function starts after short or long times. In the example shown in Fig. 4.16 the response function is well-behaved up to $t = 200$ and then diverges exponentially.

In quasi-periodic systems the echo response function $R^{(3)}(t, 0, t)$ diverged with time, making it impossible to calculate 2d spectra, but is this effect characteristic to chaotic systems, too? At high enough temperatures mostly the chaotic region is sampled and the previously observed divergence is not seen. By reducing the temperature to $\beta = 80$ the quasi-periodic region is probed more and a linear divergence similar to the one observed

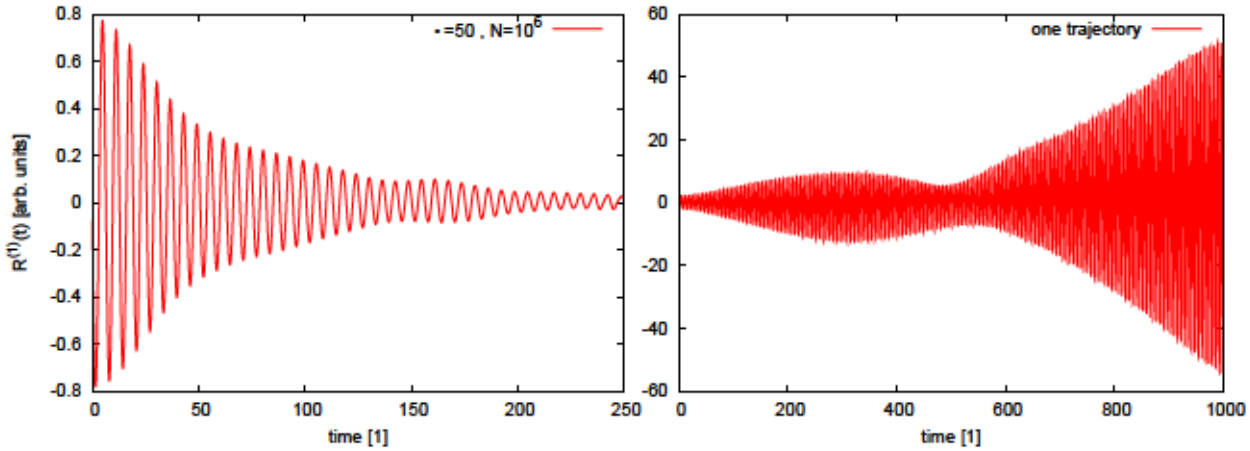

Figure 4.14.: Hénon Heiles potential: Linear response function averaged over 10^6 trajectories (left) and from one trajectory with initial conditions $x = y = 0$ and $p_x = p_y = 0.125$.

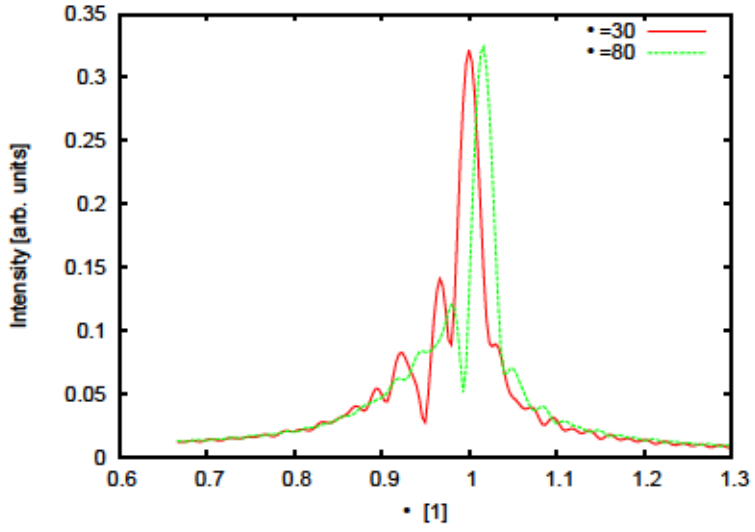

Figure 4.15.: Hénon Heiles potential: The Fourier transform of the linear response functions at $\beta = 30$ and $\beta = 80$.

in Morse potential is regained, see Fig. 4.17 for the comparison. In this respect chaotic systems are easier to handle than the quasi-periodic ones.

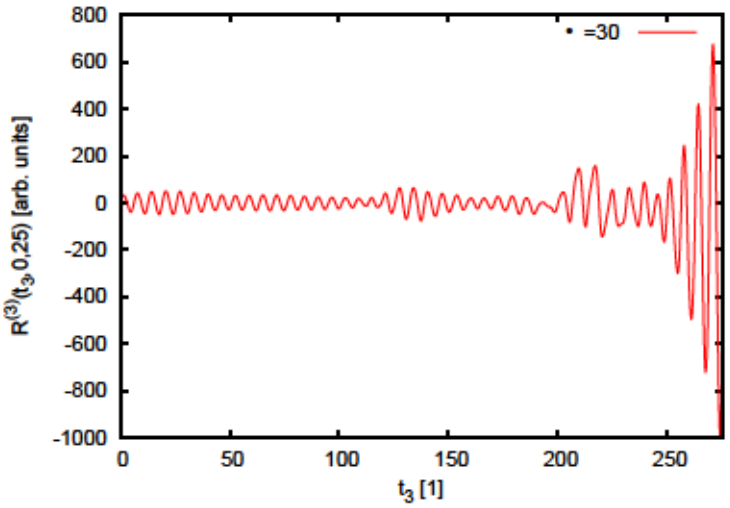

Figure 4.16.: Hénon Heiles potential: Averaged $R^{(3)}(t, 0, 25)$ with $\beta = 30$. The diverging matrix elements eventually cause a divergence of the response function, but produce a nice signal for shorter times.

Since there is no inherent divergence it is possible to calculate 2d spectra. The 2d plot in time domain has peaks with high amplitude for small times and decays in both time directions but does not vanish completely, see Fig. 4.18. Therefore before the Fourier transformation is performed an exponential cutoff is put to the data for $t_i > 40$ to ensure smooth decay to zero. The cutoffs are justified here [13], because the lack of statistics causes the response function to stay larger than zero, and increasing the statistics is computationally expensive. The real and imaginary part of the rephasing and non-rephasing signal are calculated and the real parts are shown in Fig. 4.19. The shape of the peaks in the 2d spectrum indicate the inhomogeneous limit, meaning that the dynamics is slow compared to the coupling strength [1]. The negative features are a sign of excited state absorption, which is in accordance with the additional peak in Fig. 4.15 in the chaotic regime. The aim here is not to analyze the 2d spectra of Hénon Heiles potential further but to investigate the capabilities of the used response function formalism. Thus we conclude, that response function formalism based on classical trajectories can be employed to compute 2d spectra in chaotic systems.

In summary, the linear and non-linear response functions for the Hénon Heiles potential were calculated. In the chaotic regime of the Hénon Heiles potential the exponential divergence of the stability matrix elements is canceled by averaging over Boltzmann ini-

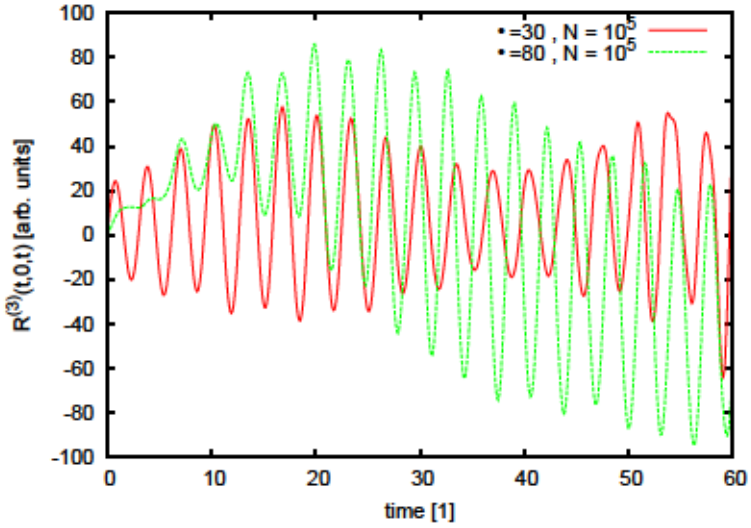

Figure 4.17.: Averaged Echo $R^{(3)}(t,0,t)$ for different temperatures. For $\beta = 30$ (red) no divergence is seen, the system is chaotic, while the response function diverges for the lower temperature $\beta = 80$ (green) up to longest trajectory calculated.

tial conditions. The resulting response function eventually diverges but the signal stays finite for long enough times to calculate spectra. Furthermore in the chaotic regime no divergence of the response function $R^{(3)}(t,0,t)$ is observed, but it appears again at lower temperatures in the quasi-periodic regime. One could call this counterintuitive effect the 'blessing of chaos', since even so the stability matrices elements diverge exponentially, meaningful non-linear response functions can be computed in the chaotic regime. In the context of molecular systems the discussed protocol can be applied, as long as the nuclei move chaotic enough and the statistics can be afforded.

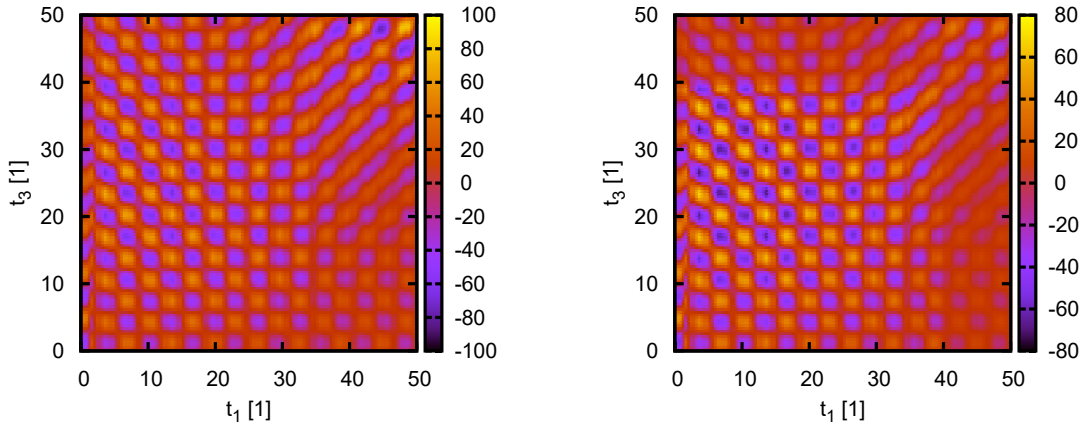

Figure 4.18.: Hénon Heiles potential: 2d visualization of the non-linear response with population time zero and $\beta = 30$ before the cutoffs are applied (left) and with the cutoffs (right).

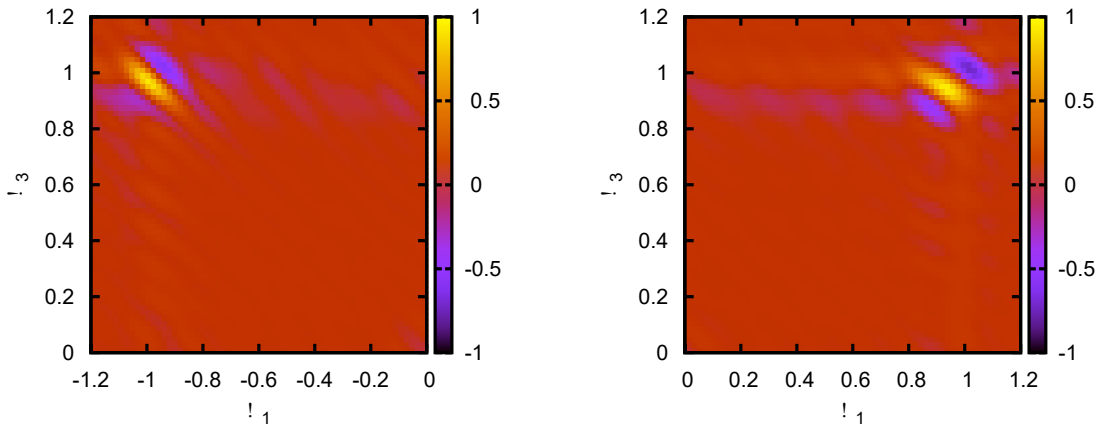

Figure 4.19.: Hénon Heiles potential: The real part of rephasing (left) and the non-rephasing (right) 2d spectrum at $\beta = 30$ normalized to the maximum value.

4.2. Ionic Liquids

Having established the methodology to calculate (non-) linear spectra and understanding the limitations, the formalism can be applied to molecular systems. Since the response functions demand huge statistical averaging, the only option is a molecular mechanics simulation based on force fields. It will be investigated if the method is applicable to the ionic liquid discussed in the introduction $[C_2mim][NTf_2]$ and if it is, then what can be learned concerning the H-bonds discussed in the introduction. The linear response is investigated by a power spectrum of the coordinate, which is an autocorrelation function 2.17, and dynamic normal modes are calculated. To draw conclusions concerning the H-bond results obtained for a gas phase cation, a pair, i.e. a single cation and a single anion, and bulk phase are compared.

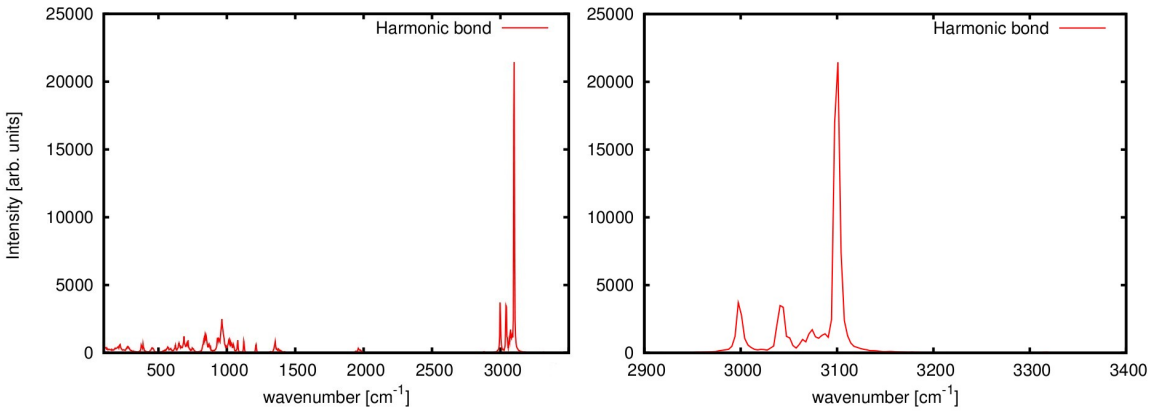

Figure 4.20.: Power spectrum of $[C_2mim][NTf_2]$ (left) and of its C-H stretch region (right).

The power spectrum in bulk with harmonic bond potentials yields C-H stretches in the right spectral region, see Fig. 4.20, with three peaks at 3000cm^{-1}, 3040cm^{-1} and 3100cm^{-1}. To investigate the stretches and assign the bands, normal mode analysis is performed using the Normcor code [24]. All three C-H stretches of interest contribute to the peak around 3100cm^{-1} as the normal modes calculated lie at 3077cm^{-1}, 3080cm^{-1} and 3094cm^{-1} . Furthermore the discussed Fermi resonance is not described by the force field, as the in-ring vibrations all lie well below 1550cm^{-1}.

In harmonic bonds the frequency can only change due to modulations of the potential, e.g. by H-bonding. By adding an anharmonic term to the bond potential the frequency shift due to H-bonding will be more pronounced since the averaged C-H bond length

increases. To model this effect the three harmonic C-H bonds on the imidazolium ring are replaced by Morse potentials with the parameters given in Tab. 3.1. Now an additional broad peak at higher wavenumbers than in the harmonic bond case is visible in the power spectrum, Fig. 4.21. In Fig. 4.22 the power spectrum of the three investigated C-H stretches can be seen. All stretch modes couple to lower frequencies. The normal mode frequencies for a single cation and a bulk phase cation are summarized in Tab. 4.1. In the gas phase cation the C(2) - H vibrates at 3308cm^{-1}, while the symmetric and antisymmetric modes of C(4/5) - H are at 3286cm^{-1} and 3298cm^{-1}, respectively. Again the C(2) is not red shifted with respect to C(4/5).

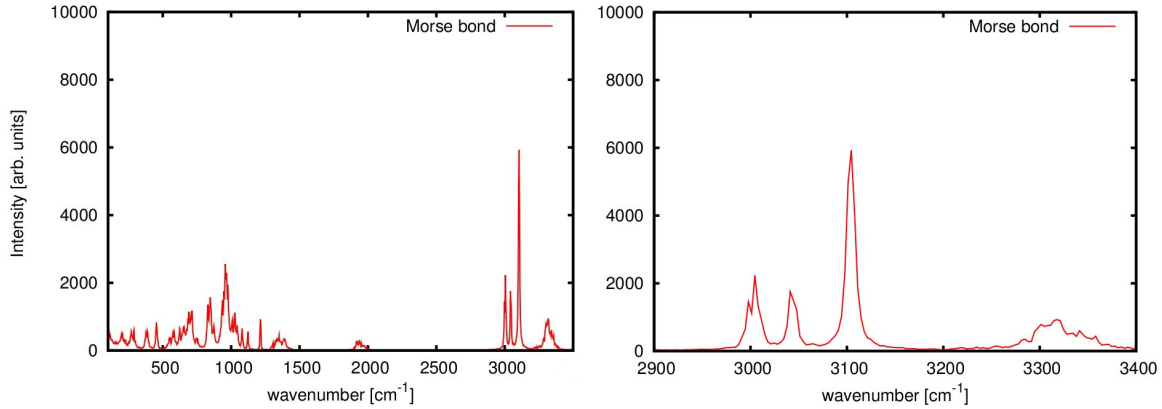

Figure 4.21.: Power spectrum of [C_2mim][NTf_2] (left) and of its C-H stretch region (right).

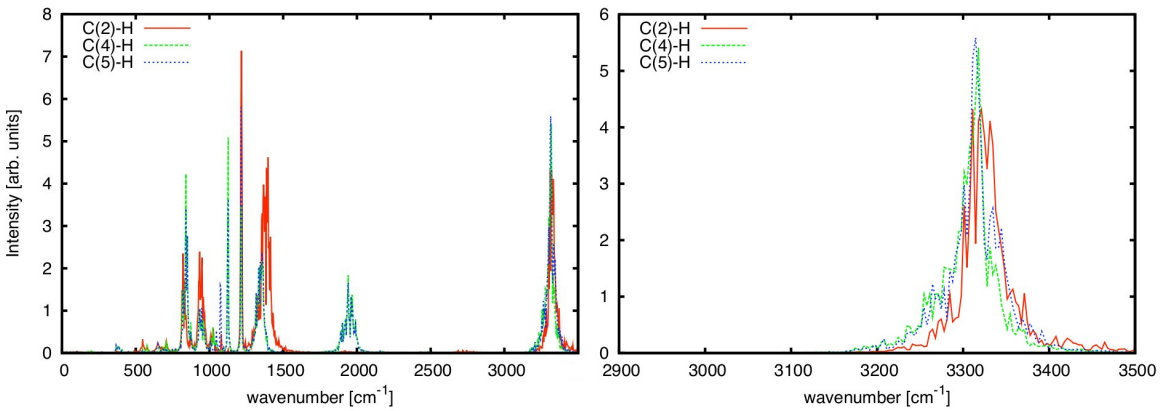

Figure 4.22.: Power spectrum of the three C-H stretches in the imidazolium ring in [C_2mim][NTf_2] of the entire spectrum (left) and the C-H stretch region (right).

	symmetric	antisymmetric	C(2)-H
bulk (harmonic)	3080 cm^{-1}	3077 cm^{-1}	3094 cm^{-1}
bulk (morse)	3311 cm^{-1}	3334 cm^{-1}	3348 cm^{-1}
single cation (morse)	3286 cm^{-1}	3298 cm^{-1}	3308 cm^{-1}
ab initio	3214 cm^{-1}	3238 cm^{-1}	3245 cm^{-1}
experiment[8]	3180cm^{-1}	3160 cm^{-1}	3120 cm^{-1}

Table 4.1.: Frequencies of the normal modes of the three C-H stretches in the imidazolium ring. Using Morse bond potentials, the frequencies from bulk calculations are considerably blue shifted to the gas phase results. The ab initio calculations are for a pair, but the modes did not decouple and are arranged with increasing value.

The resulting frequencies from the normal mode analysis of a cation in bulk are puzzling. All three C-H stretches are blue-shifted with respect to the gas phase results. A longer C-H distance, as assumed in H-bonds, means that more anharmonicity of the potential is probed and the frequency would be red-shifted. The blue-shifted frequencies thus can not be a sign for H-bonding. To investigate this behavior the effective potential along the C-H stretch is calculated and compared to the Morse bond potential. In a canonical ensemble an effective potential V_{eff} can be calculated via

$$V_{\text{eff}} = -k_B T \ln \rho. \tag{4.2}$$

The probability density of the bond length of the C-H stretch is computed and used as ρ in Eq. 4.2. The resulting potential is considerably narrower than the unmodulated Morse bond potential which explains the aforementioned blue shift, see Fig. 4.23.

But what causes the modification of the potential? Let's assume that the van der Waals force pushes the hydrogen away from the anion, possibly because the high charge in the ring brings anion and cation close together leading to a repulsive Lennard-Jones potential. The Lennard-Jones parameters are summarized in Tab. 4.2 together with the equilibrium distance r_{vdW} which is calculated from the force field parameter σ by $r_{\text{vdW}} = \sqrt[6]{2}\sigma$. In Fig. 4.24 the radial distribution function (rdf) of the C(2) hydrogen to the oxygens of the anion in a pair (= single cation single anion) simulation is shown. The rdf has a peak at 2Å to which the mean H-O distance during H-bonding is assigned. Therefore the Lennard-Jones potential is well in the repulsive regime and can therefore account for the observed modulation of the C-H potential. The Coulomb potential is of

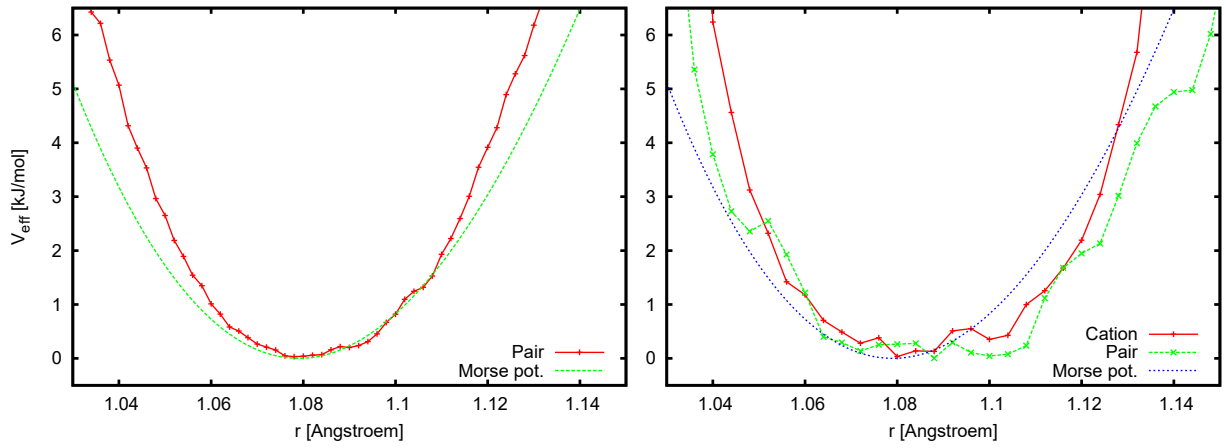

Figure 4.23.: The effective potential V_{eff} of C(2)-H stretch from MM simulation (left) is considerably narrower than the Morse bond potential(green) and from an ab initio simulation (right) using B3LYP level of theory and 6-31+gs basis for a single cation and an ion pair in gas phase.

course still attractive, but the combined minima of the two potentials is at a too large distance of the oxygen and hydrogen to describe the H-bonding correctly.

	C(2) − H	C(4/5) − H
σ_{HO}	2.24Å	2.67Å
$r_{\text{vdW}}^{(\text{HO})}$	2.51Å	3.0Å

Table 4.2.: Lennard-Jones parameter σ of the force field for C(2)-H and C(4/5)-H van der Waals interaction.

To see whether the investigated blue shift is an artifact of the force field or a real effect, the effective potentials from an ab initio simulation with 6-31+gs basis set of a pair and a single cation in gas phase are computed, see Fig. 4.23. As expected, the effective C(2)-H potential in H-bonding conformation is broader than the C-H potential of the single cation with no H-bonding. In terms of frequencies this corresponds to a red shift of all stretches involved in H-bonding. Furthermore a power spectrum of a cation in a pair is computed from one 7.5 ps ab initio trajectory, see Fig. 4.25. The Normcor code was not able to decouple the three C-H stretches and the frequencies in Tab. 4.1 are arranged from small to large values. The imidazolium C-H stretches are at

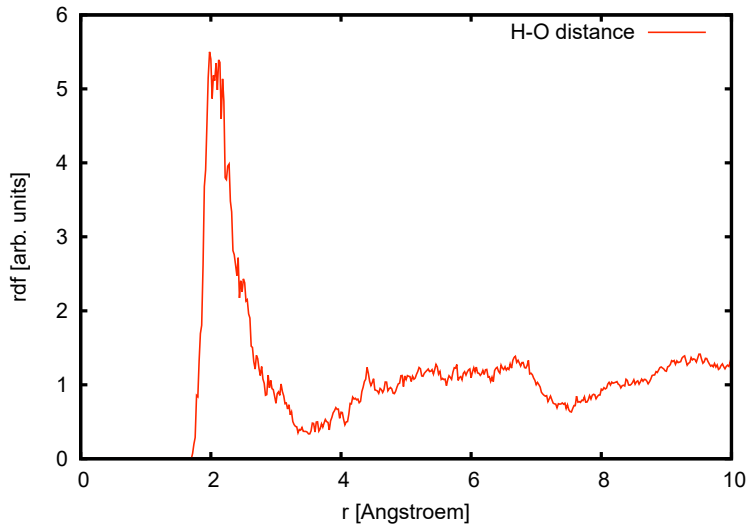

Figure 4.24.: The unnormalized radial distribution function of the hydrogen on C(2) of the cation to oxygen atoms taken from a NVT simulation of bulk.

higher frequencies than in the experiment, i.e. at around $3214 - 3245\text{cm}^{-1}$ compared to frequencies between $3120 - 3180\text{cm}^{-1}$. The wavenumber do not match quantitatively, but one has to keep in mind, that the pair in the simulation lacks the bulk effect measured in the experiment. Still the ab initio results are closer to the measured wavenumbers than the bulk simulation using Morse bond force fields. This also holds true for the in-ring vibrations now lie in the expected region around 1500cm^{-1}, making a Fermi resonance possible.

The force field has problems describing the investigated the H-bonds in ionic liquids and meaningful IR spectra cannot be calculated at the present stage. Brehm *et al.* [29] have stated very recently that: 'classical molecular simulation, that is a well-known method to represent the structure and physicochemical properties of ionic liquids [..], is known to often lack the correct description of hydrogen bonding.' In the force field used the van der Waals parameters were adjusted to reproduce macroscopic parameters like experimental values for self-diffusion coefficients, rather than to describe microscopic properties needed for the calculation of IR spectra. Accidentally harmonic C-H stretches show right behavior as compared with gas phase ab initio frequencies, but lack any physical justification. The force field preceding the used one, developed by Lopes *et al.* [28] proposes an even higher value for $\sigma_H = 2,42\text{Å}$, but no value for the anion oxygen. Keeping the oxygen parameter this force field would generate the effect even stronger. The

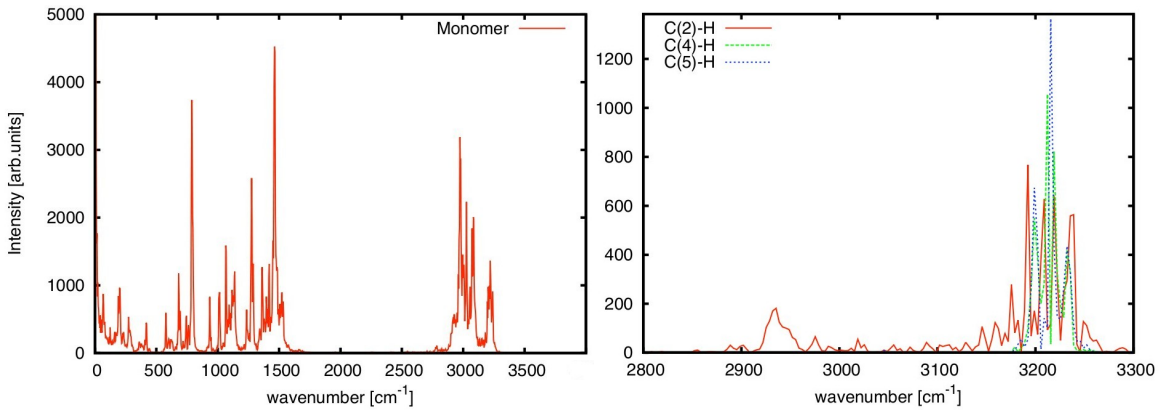

Figure 4.25.: Power spectrum of the cation calculated from a 7.5 ps Langevin dynamic trajectory obtained by ab initio calculations with 6-31+gs basis set of a pair (left) and the three investigated C-H stretches (left) only, with all contributions shown.

use of ab initio simulations is not an option because to average the response function correctly millions of trajectories have to be used which is clearly not feasible on the ab initio level. The only solution is to advance the force fields towards a correct description of H-bonds in ionic liquid.

5. Summary and Outlook

In this thesis an approach to compute (non-) linear spectra has been presented, using response functions calculated from classical trajectories. Taking the classical limit of a response function leads to stability matrices, that diverge exponentially in chaotic systems. The stability properties of the stability matrix as well as the convergence properties of the (non-) linear response functions were investigated on model quasi-periodic and chaotic systems. Due to the diverging matrix elements in chaotic systems the propagation of stability matrices is very sensitive to the numerics chosen. Contrary to the general opinion, response functions averaged over microcanonical ensembles did not converge but oscillated with high amplitude and long periods. It turns out that the linear classical response function can be computed without problem, if it is averaged over Boltzmann distributed initial conditions. The non-linear response function $R^{(3)}(t, 0, t)$ diverges linearly in Morse potential and the Hénon Heiles potential at low temperatures, but in chaotic regions of the Hénon Heiles potential it does not diverge. Meaningful 2d spectra can thus only be calculated in chaotic systems and molecular system under normal conditions are chaotic enough.

Since the response function are highly demanding with respect to the statistics, the application of this approach to molecular systems can only be done using molecular mechanics and force fields. The van der Waals parameters of the employed force field push the hydrogen away from the anion and blue shift the C-H stretch vibration. The force field fit to macroscopic observables is not suited to describe the microscopic properties in the ionic liquid. Ab initio simulations verified, that H-bond in the ionic liquids under study could not be reproduced correctly.

On the methodological side of this thesis the starting point for a development of a protocol to calculate non-linear spectra was set. In the future the application of a better algorithm, like the ones developed by Alvermann *et al.* [30] for the propagation of the stability matrix could be considered. Only response functions with population time

$t_2 = 0$ were calculated and the code should be generalized to permit finite population times. The general procedure works well, but it has to rely on force fields that describe the dynamics on the micro-scale correctly, therefore to apply it to ionic liquids the development of reliable force fields is mandatory.

A. Quantum Response Function Derivation

This appendix derives the n-order quantum response function in more detail, starting from the polarization in the interaction representation

$$P(\tau) = n_{\text{mol}} \text{Tr}\left[\hat{\rho}_{\text{eq}} \hat{S}^{\dagger}(\tau, \tau_0) \hat{\mu}^{\text{I}}(t) \hat{S}(\tau, \tau_0)\right]. \tag{A.1}$$

with the time evolution operator Eq. 2.3

$$\hat{S}(\tau\tau_0) = \hat{T} \exp\left(-\frac{i}{\hbar} \int_{\tau_0}^{t} dt' V^{\text{I}}(\tau')\right). \tag{A.2}$$

The complete polarization is a result of an perturbation expansion to infinity of the light matter interaction in the operator $\hat{S}$, but here interest lies on calculating only the individual n-th order polarization. The time operator $\hat{S}(t, t_0)$ is therefore expanded to the n-th order

$$\hat{S}(\tau, \tau_0) \rightarrow 1 + \hat{S}^{(1)}(\tau, \tau_0)) + \hat{S}^{(2)}(\tau, \tau_0) + \cdots + \hat{S}^{n}(\tau, \tau_0)$$

in the polarization

$$\begin{aligned} P(\tau) \quad = \quad & n_{\text{mol}} \text{Tr}\Big[\hat{\rho}_{\text{eq}}\Big(1 + \hat{S}^{(1)\dagger}(\tau, \tau_0) + \cdots + \hat{S}^{(n)\dagger}(\tau, \tau_0)) \\ & \hat{\mu}^{\text{I}}(t)(1 + \hat{S}^{(1)}(\tau, \tau_0) + \cdots + \hat{S}^{(n)}(\tau, \tau_0)\Big)\Big]. \end{aligned} \tag{A.3}$$

All n-th order terms are collected to calculate just the n-th order polarization

$$\begin{aligned} P^{(n)}(\tau) \quad = \quad & n_{\text{mol}} \text{Tr}\Big[\rho_{\text{eq}}\Big(\hat{S}^{(n)\dagger}(\tau, \tau_0) \hat{\mu}^{\text{I}}(\tau) 1 \\ & + \hat{S}^{(n-1)\dagger}(\tau, \tau_0) \hat{\mu}^{\text{I}}(\tau) \hat{S}^{(1)}(\tau, \tau_0) + \cdots 1 \hat{\mu}^{\text{I}}(t) \hat{S}^{(n)}(\tau, \tau_0)\Big)\Big] \end{aligned} \tag{A.4}$$

and the $\hat{S}(t,t_0)$ operator is replace by its n-th order terms where the interaction Hamiltonian is replaced by $V^{\mathrm{I}}(\tau) = -\mu^{\mathrm{I}}E(\tau)$

$$\begin{aligned} P^{(n)}(\tau) &= \left(\frac{i}{\hbar}\right)^n \int_{\tau_0}^{\tau}\cdots\int_{\tau_0}^{\tau_1} d\tau_1\cdots d\tau_n E(\tau_n)\ldots E(\tau_1)\mathrm{Tr}[\rho_{eq}(\hat{\mu}^{\mathrm{I}}(\tau_n)\ldots\hat{\mu}(\tau_1)\hat{\mu}^{\mathrm{I}}(\tau)1 - \\ &\quad \hat{\mu}^{\mathrm{I}}(\tau_{n-1})\cdots\hat{\mu}^{\mathrm{I}}(\tau_1)\hat{\mu}^{\mathrm{I}}(t)\hat{\mu}^{\mathrm{I}}(\tau_n)\cdots + 1\hat{\mu}^{\mathrm{I}}(\tau)\hat{\mu}^{\mathrm{I}}(\tau_n)\cdots\mu(\tau_1))]. \end{aligned} \tag{A.5}$$

This result is rewritten in terms of the quantum commutator $[\bullet,\bullet]$

$$\begin{aligned} P^{(n)}(\tau) &= \left(\frac{i}{\hbar}\right)^n \int_{-\infty}^{t}\cdots\int_{-\infty}^{t} d\tau_n\cdots d\tau_1 E(\tau_n)\cdots E(\tau_1) \\ &\quad \mathrm{Tr}\Big(\hat{\rho}_{\mathrm{eq}}\Big[\hat{\mu}^{\mathrm{I}}(\tau_n),\Big[\hat{\mu}^{\mathrm{I}}(\tau_{n-1}),\Big[\ldots\Big]\hat{\mu}^{\mathrm{I}}(\tau_1)\Big]\Big]\Big), \end{aligned} \tag{A.6}$$

where t_0 was replaced by $-\infty$, because the density matrix is assumed to be in equilibrium and does not evolve in time under H_0 Response functions are defined as the n-th order polarization can be written in terms of the response function $R^{(n)}(\tau,...,\tau_n)$ and n external fields E acting at times τ_i .

$$\begin{aligned} P^{(n)}(\tau) &= \int_{-\infty}^{\tau}\int_{-\infty}^{\tau_n}\ldots\int_{-\infty}^{\tau_2} d\tau_n d\tau_{n-1}\ldots d\tau_1 \\ &\quad E(\tau_1)\ldots E(\tau_n)R^{(n)}(\tau,\tau_n,\tau_{n-1},\ldots,\tau_1). \end{aligned} \tag{A.7}$$

It is more common to use time intervals as arguments, which is done in [33] by setting

$$\tau_1 = 0 \tag{A.8}$$

$$t_1 = \tau_2 - \tau_1 \tag{A.9}$$

$$\ldots = \ldots \tag{A.10}$$

$$t_n = t - \tau_n. \tag{A.11}$$

The choice for τ_1 is arbitrary and is set to zero for simplicity. The n-th order polarization term in its final form is a convolution of the n fields

$$\begin{aligned} P^{(n)}(t) &= \int_0^{\infty}\ldots\int_0^{\infty} dt_n\ldots dt_1 \\ &\quad E(t-t_n)\ldots E(t-t_n-\ldots-t_1)R^{(n)}(t_n,t_{n-1},\ldots,t_1). \end{aligned} \tag{A.12}$$

with the n-th order response function

$$R^{(n)}(t_n \ldots, t_1) = \left(\frac{i}{\hbar}\right)^n \mathrm{Tr}\left(\left[\ldots\left[\hat{\mu}^{\mathrm{I}}(t_n + \ldots + t_1), \hat{\mu}^{\mathrm{I}}(t_{n-1} + \cdots + t_1)\right]\ldots\hat{\mu}^{\mathrm{I}}(0)\right]\rho_{\mathrm{eq}}\right) \tag{A.13}$$

Bibliography

[1] S.Mukamel. *Principles of nonlinear optical spectroscopy*. Oxford University Press, 1995.

[2] P.A. Franken, A E Hill, C.W. Peters, and G Weinreich. Generation of Optical Harmonics. *Physical Review Letters*, 7(1):118–120, 1961.

[3] N Bloembergen, P S Pershan, I Introduction, A E Hill, C W Peters, G Weinreich, M Bass, P A Franken, J A Giordmaine, P D Maker, R W Terhune, M Nisenoff, C M Savage, J A Armstrong, J Ducuing, E T Whittaker, M Born, and E Wolf. Light Waves at the Boundary of Nonlinear Media. *Physical Review*, 128(2):606–622, 1962.

[4] Tobias Brixner, Jens Stenger, Harsha M Vaswani, Minhaeng Cho, Robert E Blankenship, and Graham R Fleming. Two-dimensional spectroscopy of electronic couplings in photosynthesis. *Nature*, 434(7033):625–8, March 2005.

[5] J. D. Holbrey and K. R. Seddon. Ionic Liquids. *Clean Technologies and Environmental Policy*, 1(4):223–236, December 1999.

[6] Bin Zhao, Lasse Greiner, and Walter Leitner. Cellulose solubilities in carboxylate-based ionic liquids. *RSC Advances*, 2(6):2476, 2012.

[7] Jason P Hallett and Tom Welton. Room-temperature ionic liquids: solvents for synthesis and catalysis. 2. *Chemical reviews*, 111(5):3508–76, May 2011.

[8] C Roth, S Chatzipapadopoulos, D Kerlé, F Friedriszik, M Lütgens, S Lochbrunner, O Kühn, and R Ludwig. Hydrogen Bonding in Ionic Liquids Probed by Linear and Nonlinear Vibrational Spectroscopy. *New Journal of Physics*, in press, 2012.

[9] Joseph Grondin, Jean-Claude Lassègues, Dominique Cavagnat, Thierry Buffeteau, Patrik Johansson, and Roman Holomb. Revisited vibrational assignments of imidazolium-based ionic liquids. *Journal of Raman Spectroscopy*, 42(4):733–743, April 2010.

[10] Minhaeng Cho. Coherent two-dimensional optical spectroscopy. *Chemical reviews*, 108(4):1331–1418, April 2008.

[11] Christoph Dellago and Shaul Mukamel. Simulation algorithms for multidimensional nonlinear response of classical many-body systems. *The Journal of Chemical Physics*, 119(18):9344, 2003.

[12] Volkhard May and Oliver Kühn. *Charge and Energy Transfer Dynamics in Molecular Systems*. Wiley-VCH, third, rev edition, 2011.

[13] Jonggu Jeon and Minhaeng Cho. Direct quantum mechanical/molecular mechanical simulations of two-dimensional vibrational responses: N -methylacetamide in water. *New Journal of Physics*, 12(6):065001, June 2010.

[14] W G Noid, Gregory S Ezra, and Roger F Loring. Vibrational Echoes: Dephasing, Rephasing, and the Stability of Classical Trajectories †. pages 6536–6543, 2004.

[15] Vadim Khidekel Shaul Mukamel. Classical chaos and fluctuation-dissipation relations for nonlinear response. *Physical Review E*, 53(4), 1996.

[16] Christoph Dellago and Shaul Mukamel. Simulation strategies and signatures of chaos in classical nonlinear response. *Physical Review E*, 67(3):1–4, March 2003.

[17] Maksym Kryvohuz and Jianshu Cao. Classical Divergence of Nonlinear Response Functions. *Physical Review Letters*, 96(3):2–5, January 2006.

[18] Jianlan Wu and Jianshu Cao. Linear and nonlinear response functions of the Morse oscillator: Classical divergence and the uncertainty principle. *The Journal of Chemical Physics*, 115(12):5381, 2001.

[19] Maksym Kryvohuz and Jianshu Cao. Quantum-Classical Correspondence in Response Theory. *Physical Review Letters*, 95(18):1–4, October 2005.

[20] D. Marx and Hutter. *Ab Initio Molecular Dynamics: Basic Theory and Advanced Methods*. Cambridge University Press, 2009.

[21] M Tuckerman and BJ Berne. Reversible multiple time scale molecular dynamics. *The Journal of chemical physics*, 97(August), 1992.

[22] H. Zhao and M. Du. Threshold law for escaping from the Hénon-Heiles system. *Physical Review E*, 76(2):4–7, August 2007.

[23] Paul Brumer. A variational equations approach to the onset of statistical intramolecular energy transfer. *The Journal of Chemical Physics*, 65(9):3566, 1976.

[24] Gerald Mathias and Marcel D. Baer. Generalized Normal Coordinates for the Vibrational Analysis of Molecular Dynamics Simulations. *Journal of Chemical Theory and Computation*, 7(7):2028–2039, July 2011.

[25] Gerald Mathias, Sergei D Ivanov, Alexander Witt, Marcel D Baer, and Dominik Marx. Infrared Spectroscopy of Fluxional Molecules from (ab Initio) Molecular Dynamics : Resolving Large-Amplitude Motion , Multiple Conformations , and Permutational Symmetries. *Journal of Chemical Theory and Computation*8(1):224–234 2012.

[26] Thorsten Köddermann, Dietmar Paschek, and Ralf Ludwig. Molecular dynamic simulations of ionic liquids: a reliable description of structure, thermodynamics and dynamics. *Chemphyschem : a European journal of chemical physics and physical chemistry*, 8(17):2464–70, December 2007.

[27] Florian Dommert, Katharina Wendler, Robert Berger, Luigi Delle Site, and Christian Holm. Force Fields for Studying the Structure and Dynamics of Ionic Liquids: A Critical Review of Recent Developments. *Chemphyschem : a European journal of chemical physics and physical chemistry*, pages 1625–1637, February 2012.

[28] N Canongia Lopes, Johnny Deschamps, and A H Pa. Modeling Ionic Liquids Using a Systematic All-Atom Force Field. *J.Phys.Chem B*pages 2038–2047, 2004.

[29] Martin Brehm, Henry Weber, Alfonso S Pensado, Annegret Stark, and Barbara Kirchner. Proton transfer and polarity changes in ionic liquid-water mixtures: a perspective on hydrogen bonds from ab initio molecular dynamics at the example of 1-ethyl-3-methylimidazolium acetate-water mixtures–part 1. *Physical chemistry chemical physics : PCCP*, 14(15):5030–44, April 2012.

[30] A. Alvermann and H. Fehske. High-order commutator-free exponential time-propagation of driven quantum systems. *Journal of Computational Physics*, 230(15):5930–5956, July 2011.

[31] Yun-an Yan . unpublished

[32] I.S. Ufimtsev and T.J. Martinez Quantum Chemistry on Graphical Processing Units. 3. Analytical Energy Gradients and First Principles Molecular Dynamics . *J. Chem. theory Comput.*, 5:2619, 2009.

[33] Peter Hamm and Martin Zanni Concepts and Methods of 2D Infrared Spectroscopy. *Campridge University Press* , 2011

[34] N. G. van Kampen. *Phys. Norv.*, 5:279, 1971.

[35] M. Hénon and C. Heiles. The applicability of the third integral of motion: Some numerical experiments. *Astron J.*, 69:73–79, 1964.

[36] M. J. Frisch and G. W. Trucks and H. B. Schlegel and G. E. Scuseria and M. A. Robb and J. R. Cheeseman and G. Scalmani and V. Barone and B. Mennucci and G. A. Petersson and H. Nakatsuji and M. Caricato and X. Li and H. P. Hratchian and A. F. Izmaylov and J. Bloino and G. Zheng and J. L. Sonnenberg and M. Hada and M. Ehara and K. Toyota and R. Fukuda and J. Hasegawa and M. Ishida and T. Nakajima and Y. Honda and O. Kitao and H. Nakai and T. Vreven and Montgomery, Jr., J. A. and J. E. Peralta and F. Ogliaro and M. Bearpark and J. J. Heyd and E. Brothers and K. N. Kudin and V. N. Staroverov and R. Kobayashi and J. Normand and K. Raghavachari and A. Rendell and J. C. Burant and S. S. Iyengar and J. Tomasi and M. Cossi and N. Rega and J. M. Millam and M. Klene and J. E. Knox and J. B. Cross and V. Bakken and C. Adamo and J. Jaramillo and R. Gomperts and R. E. Stratmann and O. Yazyev and A. J. Austin and R. Cammi and C. Pomelli and J. W. Ochterski and R. L. Martin and K. Morokuma and V. G. Zakrzewski and G. A. Voth and P. Salvador and J. J. Dannenberg and S. Dapprich and A. D. Daniels and A. Farkas and J. B. Foresman and J. V. Ortiz and J. Cioslowski and D. J. Fox Gaussian 09 Gaussian Inc. Wallingford CT 2009

[37] David Van Der Spoel, Erik Lindahl, Berk Hess, Gerrit Groenhof, Alan E Mark, Herman J. C. Berendsen GROMACS: Fast, flexible, and free. *Journal of Computational Chemistry*, 26(16):1701-1718, 2005.

Hiermit erklĭe ich, dass die voriegende Arbeit selbständig und nur unter Verwendung der angegebenen Quellen und Hilfsmittel angefertigt wurde.

Ich möchte mich bei Prof. O. Kühn und Dr. S. Ivanov für die vielen hilfreichen Diskussionen bedanken.